Mathematics

https://www.aimspress.com/journal/Math

AIMS Mathematics, 11(7): 21323–21354.
DOI: 10.3934/math.2026865
Received: 27 April 2026
Revised: 21 June 2026
Accepted: 03 July 2026
Published: 17 July 2026

Research article

Speed selection, front locking, and threshold-attainment laws in a nonlocal cooperative Fisher–KPP system

Sufang Han[*,†], **Zhuang Zou**[†] **and Yinglei Dong**

School of Mathematics and Computer Science, Yunnan Minzu University, Kunming, China
†Sufang Han and Zhuang Zou contributed equally to this work.

* **Correspondence:** Email: sufanghan@ymu.edu.cn.

Abstract: We investigated leading-edge spectral speed candidates, conditional front locking, and threshold-attainment laws in a two-component nonlocal cooperative Fisher–KPP system. The model couples two Fisher–KPP fronts through normalized nonlocal exchange kernels and captures how cooperative exchange can entrain components with different native propagation scales. By linearizing the traveling-wave system at the leading edge, we derived an explicit Perron–Frobenius spectral branch and defined a variational spectral candidate speed c^*. We proved that this spectral candidate is well defined, satisfies quantitative row-sum bounds, and recovers the local cooperative spectral candidate as the interaction kernels concentrate at the origin. We emphasize that c^* is a leading-edge spectral candidate rather than a fully proved nonlinear spreading or minimal wave speed in the absence of an additional linear-determinacy theorem. Under a stated front-convergence hypothesis, we then derived conditional level-set locking and phase-locking consequences: If a common-speed front with speed c^* is dynamically realized, then both components have the same asymptotic level-set speed, and their spatial offsets remain asymptotically constant. This conditional locking structure further yields an affine asymptotic law for threshold-attainment times. Finite-difference simulations with efficient nonlocal convolution compare fitted finite-time front speeds with the spectral candidate and illustrate how positive coupling collapses the late-time speed gap. The computations also show that weak coupling produces a sharply anisotropic transition layer whose local structure is modulated by kernel width and kernel shape.

Keywords: Fisher–KPP system; cooperative reaction–diffusion; nonlocal coupling; speed selection; front locking; threshold-attainment law
Mathematics Subject Classification: 35B40, 35C07, 35K57, 45K05, 65M06, 65M12

1. Introduction

The Fisher–KPP equation is a classical prototype for front propagation, linear determinacy, and minimal-speed selection in reaction–diffusion theory [1–3]. Its role extends beyond the scalar setting, since many biological, ecological, and physical propagation processes involve several interacting components rather than a single density variable. In such multi-component media, cooperative coupling may substantially alter the spreading mechanism by forcing components with distinct native propagation scales to evolve in a coordinated way. Within this framework, Weinberger et al. established conditions for linear determinacy of spreading speeds in cooperative models; Liang and Zhao developed a monotone-semiflow framework relating asymptotic spreading speeds to traveling waves; and Du et al. obtained propagation results for time–space periodic cooperative systems in multidimensional media [4–6]. A central question is, therefore, whether positive coupling merely perturbs the two uncoupled propagation modes or instead suppresses the native two-speed structure and produces a single dynamically selected locked front.

This question becomes more delicate when the interaction between components is nonlocal. Nonlocal Fisher–KPP and nonlocal dispersal models have generated rich theories of traveling waves, steady states, anisotropic dispersal, and spreading speeds. Berestycki et al. established traveling-wave and steady-state results for a nonlocal Fisher–KPP equation; Coville et al. analyzed monostable equations with anisotropic nonlocal dispersal; and Weinberger and Zhao extended a general formula for spreading speeds [7–9]. These results indicate that the structure of the interaction kernel is not merely a technical modeling detail, but may directly influence the direction and quantitative speed of propagation.

More recently, Xu et al. characterized spatial propagation in nonlocal-dispersal Fisher–KPP equations; Tian et al. investigated the stability of traveling waves for a nonlocal Fisher–KPP equation; and Du and Ni related spreading speeds in cooperative nonlocal free-boundary systems to semi-waves and a threshold condition [10–12]. Related work has also established positivity and global existence for nonlocal interacting-population models and analyzed propagation dynamics for delayed nonlocal systems in periodic habitats [13, 14].

At the computational level, Simpson and McCue presented open-source computational tools and analytical concepts for Fisher–KPP-type biological invasion models, whereas Qin et al. constructed explicit–implicit alternating difference schemes for generalized time-fractional Fisher equations [15, 16]. These studies provide practical foundations for the numerical investigation of front propagation and related transition dynamics. However, most existing work emphasizes either existence and stability theory, numerical approximation, or the qualitative behavior of a single nonlocal equation. The combined mechanism linking leading-edge spectral speed selection, cooperative front locking, and threshold-attainment laws has not been systematically developed for nonlocal cooperative Fisher–KPP systems.

In this paper, we address this gap for a two-component nonlocal cooperative Fisher–KPP system. First, by linearizing the traveling-wave equations at the leading edge, we derive a nonlocal Perron–Frobenius spectral branch and introduce a variational spectral-speed functional. The resulting quantity c^* is treated throughout the paper as a leading-edge spectral candidate speed. We prove that this candidate is well defined, quantitatively bounded, and consistent with the local cooperative spectral candidate when the interaction kernels concentrate at the origin. Second, under a standard convergent-front regime, we derive conditional level-set locking and asymptotic phase-locking consequences. More precisely, if a monotone common-speed front with speed c^* is realized dynamically, then both components propagate with the same asymptotic level-set speed and differ only by asymptotically constant shifts. Third, we transfer this conditional locking structure to threshold-attainment times and obtain a corresponding affine asymptotic hitting-time law under the same front-convergence assumptions. Finally, numerical simulations compare fitted finite-time front speeds with the spectral candidate and illustrate a sharply anisotropic weak-coupling transition whose local geometry is modulated by the width and shape of the nonlocal kernels.

The contribution of the paper is therefore twofold. Analytically, it connects the leading-edge Perron–Frobenius spectral branch with conditional spatial front-locking and temporal threshold-attainment consequences under an explicit front-convergence hypothesis. Computationally, it shows that the collapse from a native two-speed regime to an approximately locked finite-time front is not isotropic in the coupling plane: The locking layer is strongly direction-dependent and can be reshaped by nonlocal kernel effects.

2. Model, assumptions, and preliminary properties

2.1. The model and kernel assumptions

Let $u_i(x,t) \in [0,1]$, $i = 1,2$, denote two normalized interacting states. We consider the nonlocal cooperative Fisher–KPP system

$$\begin{aligned} \partial_t u_1 &= d_1 \partial_{xx} u_1 + r_1 u_1(1-u_1) + \kappa_{12}((J_{12} * u_2) - u_1), \\ \partial_t u_2 &= d_2 \partial_{xx} u_2 + r_2 u_2(1-u_2) + \kappa_{21}((J_{21} * u_1) - u_2), \end{aligned} \tag{2.1}$$

for $(x,t) \in \mathbb{R} \times (0,\infty)$, where $d_i > 0$, $r_i > 0$, and $\kappa_{ij} \geq 0$. Here,

$$(J_{ij} * v)(x) = \int_{\mathbb{R}} J_{ij}(x-y) v(y)\, dy = \int_{\mathbb{R}} J_{ij}(y) v(x-y)\, dy.$$

The nonlocal exchange terms are used as normalized cooperative entrainment terms. For example, $J_{12} * u_2$ represents the spatially averaged influence of component 2 on component 1, while the local term $-u_1$ represents relaxation of the component-1 state toward this nonlocal cooperative input. Because the kernels are normalized by $\int_{\mathbb{R}} J_{ij}(y)\, dy = 1$, the exchange term vanishes on spatially homogeneous states with $u_1 = u_2$. Thus, the coupling does not alter the homogeneous equilibria $(0,0)$ and $(1,1)$, but it can entrain two components with different native Fisher–KPP propagation scales through nonlocal cooperative exchange.

Throughout the paper, the exchange kernels satisfy

$$(H_J) \qquad J_{ij} \in L^1(\mathbb{R}), \qquad J_{ij}(y) \geq 0, \qquad \int_{\mathbb{R}} J_{ij}(y)\, dy = 1, \tag{2.2}$$

and there exists $\lambda_0 > 0$ such that

$$\widehat{J_{ij}}(\lambda) := \int_{\mathbb{R}} J_{ij}(y) e^{\lambda y}\, dy < \infty, \qquad 0 < \lambda < \lambda_0. \tag{2.3}$$

We denote by

$$\mathcal{I} := \{\lambda > 0 : \widehat{J_{ij}}(\lambda) < \infty \text{ for all } i,j \in \{1,2\}\}$$

the common positive moment domain of the exchange kernels. Assumption (2.3) only guarantees that $\mathcal{I}$ is nonempty; in general, $\mathcal{I}$ may be a finite interval. For Gaussian, shifted Gaussian, and compactly supported kernels used in the numerical experiments, $\mathcal{I} = (0, \infty)$. We use the following standard solution framework throughout the paper.

Proposition 2.1 (Solution framework, positivity, and invariant region)**.** *Let the kernels satisfy* (*HJ*)*, and let the initial data satisfy*

$$u_{i,0} \in BUC(\mathbb{R}), \qquad 0 \le u_{i,0} \le 1, \qquad i = 1, 2.$$

Then, system (2.1) *admits a unique bounded mild solution*

$$u_i \in C([0, T]; BUC(\mathbb{R})), \qquad i = 1, 2,$$

on every finite time interval $0 \le t \le T$*. If the initial data are sufficiently smooth, the solution is classical for* $t > 0$*. Moreover, the order interval*

$$[0, 1]^2 = \{(u_1, u_2) : 0 \le u_i \le 1,\ i = 1, 2\}$$

is positively invariant: if $0 \le u_{i,0} \le 1$*, then*

$$0 \le u_i(x, t) \le 1, \qquad x \in \mathbb{R},\ t \ge 0,\ i = 1, 2.$$

The semiflow is also order preserving in the usual component-wise sense on bounded time intervals: If $u_{i,0} \le v_{i,0}$ *for* $i = 1, 2$*, then the corresponding mild solutions satisfy*

$$u_i(x, t) \le v_i(x, t)$$

for all $x \in \mathbb{R}$*,* $0 \le t \le T$*, and* $i = 1, 2$*.*

Proof. For $u_j \in BUC(\mathbb{R})$, the convolution terms $J_{ij} * u_j$ are well defined because $J_{ij} \in L^1(\mathbb{R})$, and

$$\|J_{ij} * u_j\|_\infty \le \|J_{ij}\|_{L^1} \|u_j\|_\infty = \|u_j\|_\infty.$$

The reaction and exchange terms are locally Lipschitz on bounded subsets of $BUC(\mathbb{R})^2$. Standard semilinear parabolic theory therefore gives a unique bounded mild solution on finite time intervals, and classical regularity for smooth initial data.

It remains to justify the invariant region. Suppose first that u_i touches the lower boundary 0 at a first contact point. At such a point, the diffusion term is nonnegative, the Fisher–KPP reaction term $r_i u_i(1 - u_i)$ vanishes, and the exchange term has the form

$$\kappa_{ij}(J_{ij} * u_j - u_i) = \kappa_{ij}(J_{ij} * u_j) \ge 0,$$

provided $u_j \ge 0$. Hence, the vector field points inward at the lower boundary. Similarly, if u_i touches the upper boundary 1, then the diffusion term is nonpositive, the Fisher–KPP reaction term again vanishes, and, using $0 \le u_j \le 1$ and $\int_{\mathbb{R}} J_{ij}(y)\, dy = 1$,

$$J_{ij} * u_j \le 1, \qquad \kappa_{ij}(J_{ij} * u_j - u_i) \le 0.$$

Thus, the vector field points inward at the upper boundary. The parabolic maximum principle gives the positive invariance of $[0, 1]^2$.

Finally, the system is cooperative because the cross-component exchange terms $J_{ij} * u_j$ enter with nonnegative coefficients $\kappa_{ij} \ge 0$. The standard comparison principle for cooperative semilinear parabolic systems yields the stated order preservation. □

The positivity and invariance statements used below are understood in this mild/classical solution framework. The normalization in (2.2) preserves the homogeneous equilibria $(0,0)$ and $(1,1)$, while the exponential moment condition (2.3) is used in the leading-edge spectral analysis. Together with Proposition 2.1, this also ensures that the biologically relevant order interval $[0,1]^2$ is invariant for normalized nonnegative kernels. When $J_{12}, J_{21} \rightharpoonup \delta_0$, system (2.1) formally reduces to the local cooperative Fisher–KPP pair. In the uncoupled case $\kappa_{12} = \kappa_{21} = 0$, the two scalar benchmark speeds are

$$c_i^* = 2\sqrt{d_i r_i}, \qquad i = 1,2. \tag{2.4}$$

For the numerical experiments, we mainly use Gaussian kernels

$$J_{ij}(y) = \frac{1}{\sqrt{2\pi}\,\sigma_{ij}} \exp\left(-\frac{y^2}{2\sigma_{ij}^2}\right), \qquad \sigma_{ij} > 0, \tag{2.5}$$

whose exponential moments are

$$\widehat{J_{ij}}(\lambda) = \exp\left(\frac{\sigma_{ij}^2 \lambda^2}{2}\right). \tag{2.6}$$

With this normalization, $\int_{\mathbb{R}} J_{ij}(y)\,dy = 1$, and therefore, the Gaussian kernels are consistent with the standing kernel assumption (HJ). To test directional nonlocality, we also use shifted Gaussian kernels

$$J_{ij}^{(m)}(y) = \frac{1}{\sqrt{2\pi}\,\sigma_{ij}} \exp\left(-\frac{(y-m_{ij})^2}{2\sigma_{ij}^2}\right), \qquad m_{ij} \in \mathbb{R}, \tag{2.7}$$

for which

$$\widehat{J_{ij}^{(m)}}(\lambda) = \exp\left(m_{ij}\lambda + \frac{\sigma_{ij}^2 \lambda^2}{2}\right). \tag{2.8}$$

We also use a normalized compactly supported kernel in the numerical kernel-shape comparison. For a prescribed width parameter $\sigma_{ij} > 0$, let

$$a_{ij} := \sqrt{3}\,\sigma_{ij}, \qquad J_{ij}^{\mathrm{cs}}(y) := \frac{1}{2a_{ij}} \mathbf{1}_{[-a_{ij}, a_{ij}]}(y).$$

Then $J_{ij}^{\mathrm{cs}} \geq 0$, $\int_{\mathbb{R}} J_{ij}^{\mathrm{cs}}(y)\,dy = 1$, and its exponential moment is

$$\widehat{J_{ij}^{\mathrm{cs}}}(\lambda) = \int_{\mathbb{R}} J_{ij}^{\mathrm{cs}}(y) e^{\lambda y}\,dy = \frac{\sinh(a_{ij}\lambda)}{a_{ij}\lambda}, \qquad \lambda > 0.$$

The choice $a_{ij} = \sqrt{3}\sigma_{ij}$ gives the compactly supported kernel the same variance scale σ_{ij}^2 as the centered Gaussian kernel.

2.2. Positivity and invariant region

The following elementary property fixes the natural state space for the subsequent front analysis.

Proposition 2.2. *The constant states* $(0,0)$ *and* $(1,1)$ *are homogeneous equilibria of* (2.1). *Moreover, if* $u_{i,0} \in L^\infty(\mathbb{R})$ *satisfies*

$$0 \le u_{i,0}(x) \le 1 \qquad \text{for a.e. } x \in \mathbb{R}, \quad i = 1,2,$$

then the corresponding bounded classical solution satisfies

$$0 \le u_i(x,t) \le 1 \qquad \text{for all } (x,t) \in \mathbb{R}\times[0,\infty), \quad i = 1,2.$$

Thus, the box $[0,1]^2$ *is positively invariant.*

Proof. By (2.2), $(J_{ij} * 0)(x) = 0$ and $(J_{ij} * 1)(x) = 1$. Hence, both $(0,0)$ and $(1,1)$ are equilibria. The off-diagonal maps

$$v \mapsto \kappa_{12}(J_{12} * v), \qquad v \mapsto \kappa_{21}(J_{21} * v)$$

are positivity-preserving, so (2.1) is cooperative. Moreover, $(0,0)$ is a subsolution, and $(1,1)$ is a supersolution. The comparison principle for cooperative semilinear parabolic systems then gives

$$0 \le u_i(x,t) \le 1, \qquad i = 1,2,$$

for all later times. □

2.3. Traveling-frame formulation

We seek traveling fronts

$$u_i(x,t) = U_i(\xi), \qquad \xi = x - ct, \tag{2.9}$$

connecting

$$(U_1,U_2)(-\infty) = (1,1), \qquad (U_1,U_2)(+\infty) = (0,0). \tag{2.10}$$

Define the profile convolution operator

$$\mathcal{J}_{ij}[U_j](\xi) := \int_{\mathbb{R}} J_{ij}(y)U_j(\xi - y)\,dy. \tag{2.11}$$

Substituting (2.9) into (2.1) gives

$$\begin{aligned} d_1U_1'' + cU_1' + r_1U_1(1-U_1) + \kappa_{12}(\mathcal{J}_{12}[U_2] - U_1) &= 0,\\ d_2U_2'' + cU_2' + r_2U_2(1-U_2) + \kappa_{21}(\mathcal{J}_{21}[U_1] - U_2) &= 0. \end{aligned} \tag{2.12}$$

This traveling-frame system is the starting point for the leading-edge linearization and the spectral speed-selection analysis.

3. Leading-edge spectral candidate in the nonlocal model

3.1. Leading-edge linearization

We derive the leading-edge spectral object associated with (2.12). Let

$$\mathcal{I} := \left\{\lambda > 0 : \widehat{J}_{12}(\lambda) < \infty,\ \widehat{J}_{21}(\lambda) < \infty\right\}. \tag{3.1}$$

By (2.3), $\mathcal{I} \neq \emptyset$; for the Gaussian and shifted Gaussian kernels defined in (2.5) and (2.7), $\mathcal{I} = (0, \infty)$.

Near the unstable state $(0, 0)$, take exponential tails

$$U_i(\xi) \sim a_i e^{-\lambda\xi}, \qquad a_i > 0, \quad \lambda \in \mathcal{I}. \tag{3.2}$$

Then

$$\mathcal{J}_{ij}[U_j](\xi) \sim a_j e^{-\lambda\xi} \widehat{J}_{ij}(\lambda).$$

Substitution into the linearization of (2.12) at $(0, 0)$ gives the leading-edge matrix

$$A(\lambda) = \begin{pmatrix} d_1\lambda^2 + r_1 - \kappa_{12} & \kappa_{12}\widehat{J}_{12}(\lambda) \\ \kappa_{21}\widehat{J}_{21}(\lambda) & d_2\lambda^2 + r_2 - \kappa_{21} \end{pmatrix}. \tag{3.3}$$

Writing

$$a_1(\lambda) = d_1\lambda^2 + r_1 - \kappa_{12}, \qquad a_2(\lambda) = d_2\lambda^2 + r_2 - \kappa_{21}, \tag{3.4}$$

the matrix $A(\lambda)$ is a 2×2 Metzler matrix whose principal branch provides a leading-edge spectral speed candidate.

3.2. The principal branch and a variational spectral-speed candidate

For $\lambda \in \mathcal{I}$, define

$$\mu(\lambda) := \rho_{\mathrm{PF}}(A(\lambda)). \tag{3.5}$$

Since $A(\lambda)$ is 2×2, its Perron–Frobenius branch is

$$\mu(\lambda) = \frac{a_1(\lambda) + a_2(\lambda) + \sqrt{(a_1(\lambda) - a_2(\lambda))^2 + 4\kappa_{12}\kappa_{21}\widehat{J}_{12}(\lambda)\widehat{J}_{21}(\lambda)}}{2}. \tag{3.6}$$

Theorem 3.1 (Continuity and positivity of the principal branch)**.** *Assume* (2.2) *and* (2.3)*. Then $\lambda \mapsto \mu(\lambda)$ is continuous on $\mathcal{I}$. If $\kappa_{12}\kappa_{21} > 0$, then $A(\lambda)$ is irreducible Metzler for every $\lambda \in \mathcal{I}$; hence, $\mu(\lambda)$ is a simple real eigenvalue with a strictly positive eigenvector.*

Proof. The map $\lambda \mapsto \widehat{J}_{ij}(\lambda)$ is continuous on compact subintervals of $\mathcal{I}$ by dominated convergence. Thus, the entries of $A(\lambda)$, and hence the eigenvalue $\mu(\lambda)$ in (3.6), depend continuously on λ. If $\kappa_{12}\kappa_{21} > 0$, the off-diagonal entries of $A(\lambda)$ are strictly positive because $J_{ij} \geq 0$, $J_{ij} \not\equiv 0$, and $\widehat{J}_{ij}(\lambda) > 0$. Therefore, $A(\lambda)$ is irreducible Metzler, and the Perron–Frobenius theorem gives the stated simplicity and positivity. □

Remark 3.2 (Reducible one-way coupling cases)**.** *The strict Perron–Frobenius positivity statement in Theorem 3.1 is used only when $\kappa_{12}\kappa_{21} > 0$. In the numerical scans below, we also include boundary slices such as $\kappa_{12} = 0$ or $\kappa_{21} = 0$. On these slices, the leading-edge matrix is reducible, and the principal spectral value should be interpreted as the spectral bound of a triangular Metzler matrix rather than as an irreducible Perron–Frobenius eigenvalue with a strictly positive eigenvector. Specifically, if $\kappa_{12} = 0$, then*

$$A(\lambda) = \begin{pmatrix} d_1\lambda^2 + r_1 & 0 \\ \kappa_{21}\widehat{J}_{21}(\lambda) & d_2\lambda^2 + r_2 - \kappa_{21} \end{pmatrix},$$

and hence

$$\mu(\lambda) = \max\{d_1\lambda^2 + r_1,\ d_2\lambda^2 + r_2 - \kappa_{21}\}.$$

Similarly, if $\kappa_{21} = 0$*, then*

$$\mu(\lambda) = \max\{d_1\lambda^2 + r_1 - \kappa_{12},\ d_2\lambda^2 + r_2\}.$$

Thus branch, switching may occur at crossings of the diagonal branches, and differentiability with respect to the coupling parameters is not asserted at such points. The one-way entrainment phenomena observed in the simulations should therefore be interpreted as forced downstream front response in reducible or nearly reducible regimes, rather than as a consequence of an irreducible Perron–Frobenius locking theorem.

Define

$$\Phi(\lambda) := \frac{\mu(\lambda)}{\lambda}, \qquad \lambda \in I, \tag{3.7}$$

and the leading-edge spectral candidate speed

$$c^* := \inf_{\lambda \in I} \Phi(\lambda). \tag{3.8}$$

Throughout the paper, c^* denotes this spectral candidate speed. If $\mathcal{I} \neq (0, \infty)$, the infimum is understood over the finite positive moment domain $\mathcal{I}$, and no interior minimizer is asserted without an additional endpoint or compactness assumption. Results that use a minimizer λ_* are therefore stated only under an explicit interior-attainment assumption. We do not claim in this section that c^* is the nonlinear spreading speed or the minimal traveling-wave speed of the full nonlocal cooperative system. Such an identification would require additional linear-determinacy, traveling-front existence, and nonlinear spreading results. The subsequent analytical locking and hitting-time statements are therefore formulated as conditional consequences under an explicit front-convergence hypothesis.

Theorem 3.3 (Attainment of the spectral candidate under a full moment domain)**.** *Assume* (2.2)–(2.3) *and* $\mathcal{I} = (0, \infty)$*. Then*

$$\Phi(\lambda) \to +\infty \quad \text{as } \lambda \downarrow 0 \quad \text{and as } \lambda \to \infty.$$

Consequently, the spectral candidate speed is attained: there exists $\lambda^* \in (0, \infty)$ *such that*

$$c^* = \Phi(\lambda^*) = \min_{\lambda > 0} \Phi(\lambda).$$

Moreover, for every $\lambda > 0$*, define*

$$\Psi_1(\lambda) := d_1\lambda + \frac{r_1 + \kappa_{12}(\widehat{J_{12}}(\lambda) - 1)}{\lambda}, \qquad \Psi_2(\lambda) := d_2\lambda + \frac{r_2 + \kappa_{21}(\widehat{J_{21}}(\lambda) - 1)}{\lambda}.$$

Then

$$\min\{\Psi_1(\lambda), \Psi_2(\lambda)\} \le \Phi(\lambda) \le \max\{\Psi_1(\lambda), \Psi_2(\lambda)\}. \tag{3.9}$$

Proof. Choose $\eta > 0$ so that $A(\lambda) + \eta I \ge 0$. The Perron root of the nonnegative matrix $A(\lambda) + \eta I$ is bounded between its minimum and maximum row sums. Since

$$\rho(A(\lambda) + \eta I) = \mu(\lambda) + \eta,$$

we obtain

$$\min_{i=1,2} \left\{ d_i\lambda^2 + r_i + \kappa_{ij}(\widehat{J_{ij}}(\lambda) - 1) \right\} \le \mu(\lambda) \le \max_{i=1,2} \left\{ d_i\lambda^2 + r_i + \kappa_{ij}(\widehat{J_{ij}}(\lambda) - 1) \right\},$$

with $j \neq i$. Dividing by λ gives (3.9).

As $\lambda \downarrow 0$, $\widehat{J_{ij}}(\lambda) \to 1$, so

$$A(\lambda) \to A(0) = \begin{pmatrix} r_1 - \kappa_{12} & \kappa_{12} \\ \kappa_{21} & r_2 - \kappa_{21} \end{pmatrix}.$$

The row sums of $A(0)$ are r_1 and r_2, hence $\mu(0) \geq \min\{r_1, r_2\} > 0$. Therefore, $\Phi(\lambda) \to +\infty$ as $\lambda \downarrow 0$.

As $\lambda \to \infty$, (3.6) implies

$$\mu(\lambda) \geq \max\{a_1(\lambda), a_2(\lambda)\} \geq \max\{d_1\lambda^2 + r_1 - \kappa_{12},\ d_2\lambda^2 + r_2 - \kappa_{21}\}.$$

Since $d_i > 0$, $\Phi(\lambda) \to +\infty$ as $\lambda \to \infty$. The continuity of Φ from Theorem 3.1 then yields the existence of a minimizer by the Weierstrass theorem. □

Remark 3.4 (Finite moment domains). *If the common moment domain is finite, for example $\mathcal{I} = (0, \lambda_0)$, the spectral candidate remains defined by*

$$c^* = \inf_{\lambda \in \mathcal{I}} \Phi(\lambda).$$

However, the infimum may be approached at the endpoint λ_0, and an interior minimizer need not exist without additional assumptions on the endpoint behavior of Φ. In this finite-domain case, the row-sum bounds remain valid for every $\lambda \in \mathcal{I}$, but the attainment statement in Theorem 3.3 is not asserted. All later formulas involving a minimizing λ^* are to be read under the explicit assumption that such a minimizer is unique, interior, and smooth with respect to the relevant parameters.

For Gaussian kernels, $\widehat{J_{ij}}(\lambda) = \exp(\sigma_{ij}^2\lambda^2/2) \geq 1$, so (3.9) shows explicitly how the nonlocal interaction scale enters the spectral-candidate bounds.

3.3. Local-limit consistency

We next verify that the nonlocal spectral construction converges to the local cooperative spectral candidate when the kernels concentrate at the origin. Let $\{J_{ij}^{(\sigma)}\}_{\sigma>0}$ satisfy (2.2)–(2.3) and assume

$$\widehat{J}_{ij}^{(\sigma)}(\lambda) \to 1 \qquad \text{locally uniformly for } \lambda \in (0, \infty) \quad \text{as } \sigma \downarrow 0. \tag{3.10}$$

Define

$$A_\sigma(\lambda) = \begin{pmatrix} d_1\lambda^2 + r_1 - \kappa_{12} & \kappa_{12}\widehat{J}_{12}^{(\sigma)}(\lambda) \\ \kappa_{21}\widehat{J}_{21}^{(\sigma)}(\lambda) & d_2\lambda^2 + r_2 - \kappa_{21} \end{pmatrix}, \tag{3.11}$$

and

$$\mu_\sigma(\lambda) := \rho_{\mathrm{PF}}(A_\sigma(\lambda)), \qquad \Phi_\sigma(\lambda) := \frac{\mu_\sigma(\lambda)}{\lambda}, \qquad c_*^{(\sigma)} := \inf_{\lambda>0} \Phi_\sigma(\lambda). \tag{3.12}$$

The local counterparts are

$$A_{\mathrm{loc}}(\lambda) = \begin{pmatrix} d_1\lambda^2 + r_1 - \kappa_{12} & \kappa_{12} \\ \kappa_{21} & d_2\lambda^2 + r_2 - \kappa_{21} \end{pmatrix}, \tag{3.13}$$

and

$$\mu_{\mathrm{loc}}(\lambda) := \rho_{\mathrm{PF}}(A_{\mathrm{loc}}(\lambda)), \qquad \Phi_{\mathrm{loc}}(\lambda) := \frac{\mu_{\mathrm{loc}}(\lambda)}{\lambda}, \qquad c_*^{\mathrm{loc}} := \inf_{\lambda>0} \Phi_{\mathrm{loc}}(\lambda). \tag{3.14}$$

We next record the local-limit consistency of the spectral construction for normalized concentrating kernels. This statement is formulated at the level of the moment functions. In particular, it applies to the normalized Gaussian kernels in (2.5) for which

$$\widehat{J}_{ij}^{(\sigma)}(\lambda) = \exp\left(\frac{\sigma_{ij}^2\lambda^2}{2}\right) \to 1$$

locally uniformly in λ as $\sigma_{ij} \to 0$. For shifted Gaussian kernels, the same conclusion holds when $\sigma_{ij} \to 0$ and $m_{ij} \to 0$, since

$$\widehat{J}_{ij}^{(\sigma,m)}(\lambda) = \exp\left(m_{ij}\lambda + \frac{\sigma_{ij}^2\lambda^2}{2}\right) \to 1$$

locally uniformly on compact λ-intervals.

Proposition 3.5 (Local-limit consistency for normalized concentrating kernels)**.** *Let $J_{ij}^{(\eta)}$ be a family of normalized kernels satisfying (HJ), and assume that*

$$\widehat{J}_{ij}^{(\eta)}(\lambda) \to 1$$

locally uniformly on compact subintervals of the common moment domain as $\eta \to 0$, for all $i, j \in \{1, 2\}$. Let $A_\eta(\lambda)$, $\mu_\eta(\lambda)$, and $\Phi_\eta(\lambda) = \mu_\eta(\lambda)/\lambda$ denote the corresponding nonlocal leading-edge matrix, spectral branch, and spectral-speed functional. Let $A_0(\lambda)$, $\mu_0(\lambda)$, and $\Phi_0(\lambda)$ be the local cooperative counterparts obtained by replacing $\widehat{J}_{ij}^{(\eta)}(\lambda)$ with 1. Then

$$A_\eta(\lambda) \to A_0(\lambda), \qquad \mu_\eta(\lambda) \to \mu_0(\lambda), \qquad \Phi_\eta(\lambda) \to \Phi_0(\lambda),$$

locally uniformly in λ. Consequently, on any compact interval containing an isolated interior minimizer of Φ_0, the corresponding spectral candidate speeds converge:

$$c_\eta^* \to c_0^*,$$

provided the minimizing points remain in that compact interval.

Proof. The convergence $A_\eta(\lambda) \to A_0(\lambda)$ follows directly from the locally uniform convergence of the moment functions. Since eigenvalues of a 2×2 matrix depend continuously on the matrix entries, the principal spectral branches satisfy $\mu_\eta \to \mu_0$ locally uniformly. Dividing by λ gives the locally uniform convergence of Φ_η on compact subintervals away from $\lambda = 0$. The convergence of the minimized spectral candidates under the stated compact interior-minimizer condition is the standard stability of isolated minimizers under locally uniform convergence. □

Therefore, the corrected Gaussian and shifted Gaussian families used in the numerical experiments satisfy the local-limit hypothesis above whenever the width parameters tend to zero and, in the shifted case, the shifts also tend to zero. For the Gaussian family with $\sigma_{ij} = \alpha_{ij}\sigma$, one has

$$\widehat{J}_{ij}^{(\sigma)}(\lambda) = \exp\left(\frac{\alpha_{ij}^2\sigma^2\lambda^2}{2}\right) \to 1 \qquad \text{locally uniformly on } (0, \infty),$$

so Proposition 3.5 applies directly to the kernels used in the numerical experiments.

4. Conditional front-locking and threshold-attainment consequences

4.1. A front-convergence hypothesis

We now examine the consequences of the leading-edge spectral candidate speed c^* under an explicit front-convergence hypothesis. The results in this section are not intended to prove nonlinear speed selection, global spreading, or traveling-front convergence for the full nonlocal cooperative system. Instead, they show that if a monotone common-speed front with speed c^* is dynamically realized, then its level sets, phase offsets, and threshold-attainment times obey explicit asymptotic laws. Assume that there exists a monotone traveling front

$$U = (U_1, U_2), \tag{4.1}$$

with speed c_*, connecting $(1, 1)$ to $(0, 0)$, such that for some $\xi_0 \in \mathbb{R}$ and every $R > 0$,

$$\sup_{|\xi|\le R} |u_i(\xi + c_* t, t) - U_i(\xi - \xi_0)| \to 0 \qquad \text{as } t \to \infty, \quad i = 1, 2. \tag{4.2}$$

This is a front-convergence hypothesis rather than a front-locking theorem. Under this hypothesis, the common speed c^* is already built into the limiting traveling front. Therefore, the results below should be interpreted as conditional consequences of the assumed convergence, not as an independent proof that the nonlocal cooperative system always selects or converges to such a front. The purpose of the analysis is to make precise the level-set, phase-offset, and threshold-attainment implications once such a common-speed front has been realized. To make the global level-set definition used below compatible with the local moving-frame convergence in (4.2), we also impose a main-front admissibility condition: For each $i = 1, 2$, there exists $T_0 > 0$ such that $x \mapsto u_i(x, t)$ is nonincreasing on $\mathbb{R}$ for all $t \ge T_0$. This condition rules out detached super-level bumps far ahead of the main front. Equivalently for the arguments below, it may be replaced by any uniform ahead-of-front exclusion condition ensuring that the rightmost h-level set belongs to the main transition zone for all sufficiently large time.

4.2. Conditional level-set and phase locking

For $h \in (0, 1)$, define the level-set location

$$X_i^{(h)}(t) := \sup\{x \in \mathbb{R} : u_i(x, t) \ge h\}, \qquad i = 1, 2. \tag{4.3}$$

Under the main-front admissibility condition, this global supremum coincides with the rightmost crossing of the main monotone transition layer for all sufficiently large t. The following result records the level-set consequence of the front-convergence hypothesis.

Theorem 4.1 (Conditional level-set locking)**.** *Assume that* (4.2) *and the main-front admissibility condition above hold, and suppose that each U_i is strictly decreasing on $\mathbb{R}$. Then, for every $h \in (0, 1)$,*

$$\beta_i^{(h)} := \xi_0 + U_i^{-1}(h), \qquad i = 1, 2, \tag{4.4}$$

is well defined and

$$X_i^{(h)}(t) = c_* t + \beta_i^{(h)} + o(1) \qquad \textit{as } t \to \infty. \tag{4.5}$$

In particular,

$$\lim_{t\to\infty} \frac{X_i^{(h)}(t)}{t} = c_*, \qquad i = 1, 2. \tag{4.6}$$

Proof. Let $\xi_i^{(h)} = U_i^{-1}(h)$. For any $\varepsilon > 0$,

$$U_i(\xi_i^{(h)} - \varepsilon) > h > U_i(\xi_i^{(h)} + \varepsilon).$$

Using (4.2), for all sufficiently large t,

$$u_i(c_* t + \xi_0 + \xi_i^{(h)} - \varepsilon, t) > h, \qquad u_i(c_* t + \xi_0 + \xi_i^{(h)} + \varepsilon, t) < h.$$

By the main-front admissibility condition, $u_i(\cdot, t)$ is nonincreasing for all sufficiently large t. Hence, the second inequality implies that

$$u_i(x, t) < h \quad \text{for all } x \geq c_* t + \xi_0 + \xi_i^{(h)} + \varepsilon,$$

while the first inequality shows that the h-superlevel set reaches at least $c_* t + \xi_0 + \xi_i^{(h)} - \varepsilon$. Thus

$$c_* t + \xi_0 + \xi_i^{(h)} - \varepsilon \leq X_i^{(h)}(t) \leq c_* t + \xi_0 + \xi_i^{(h)} + \varepsilon.$$

Since $\varepsilon > 0$ is arbitrary, (4.5) follows. Dividing by t gives (4.6). □

Theorem 4.2 (Conditional phase locking)**.** *Under the assumptions of Theorem 4.1, for every $h \in (0, 1)$,*

$$X_1^{(h)}(t) - X_2^{(h)}(t) = \beta_1^{(h)} - \beta_2^{(h)} + o(1) \qquad \text{as } t \to \infty. \tag{4.7}$$

Consequently,

$$\frac{X_1^{(h)}(t) - X_2^{(h)}(t)}{t} \to 0, \qquad \text{as } t \to \infty, \tag{4.8a}$$

$$\frac{X_1^{(h)}(t)}{X_2^{(h)}(t)} \to 1, \qquad \text{as } t \to \infty. \tag{4.8b}$$

Proof. The result follows by subtracting the two expansions in (4.5). The ratio limit follows because $c_* > 0$. □

Thus, under the front-convergence hypothesis, the two components share the same asymptotic level-set speed and differ only by a threshold-dependent phase shift. This conclusion is conditional on the realization of the common-speed front in (4.2).

4.3. Conditional threshold-attainment laws

To pass from level-set locations to hitting times, we use one additional main-front crossing condition. For each fixed $h \in (0, 1)$ and $i = 1, 2$, assume that there exists $T_h > 0$ such that $X_i^{(h)}(t)$ is nondecreasing for $t \geq T_h$ and $X_i^{(h)}(t) \to +\infty$ as $t \to \infty$. Equivalently, sufficiently far spatial points encounter the h-level of the main front through a single nonreceding crossing. Together with the spatial main-front admissibility condition in Section 4.1, this ensures that, for all sufficiently large x^*, the hitting time is the generalized inverse of the rightmost level-set location:

$$\tau_i^{(h)}(x^*) = \inf\{t \geq T_h : X_i^{(h)}(t) \geq x^*\}.$$

For $x^* \in \mathbb{R}$ and $h \in (0, 1)$, define

$$\tau_i^{(h)}(x^*) := \inf\{t \geq 0 : u_i(x^*, t) \geq h\}, \qquad i = 1, 2. \tag{4.9}$$

Corollary 4.3 (Conditional threshold-attainment law)**.** *Assume the hypotheses of Theorem 4.1 and the main-front crossing condition above. Then*

$$\tau_i^{(h)}(x^*) = \frac{x^* - \beta_i^{(h)}}{c_*} + o(1) \quad \textit{as } x^* \to +\infty.$$

Proof. Write

$$X_i^{(h)}(t) = c_* t + \beta_i^{(h)} + r_i(t), \qquad r_i(t) \to 0 \quad \text{as } t \to \infty,$$

as given by Theorem 4.1. Fix $\delta > 0$ and define

$$t_-(x^*) = \frac{x^* - \beta_i^{(h)}}{c_*} - \delta, \qquad t_+(x^*) = \frac{x^* - \beta_i^{(h)}}{c_*} + \delta.$$

Since $x^* \to +\infty$, both $t_-(x^*)$ and $t_+(x^*)$ tend to $+\infty$. Hence, for all sufficiently large x^*,

$$|r_i(t_-(x^*))| + |r_i(t_+(x^*))| < \frac{c_*\delta}{2}.$$

Therefore,

$$X_i^{(h)}(t_-(x^*)) \leq x^* - \frac{c_*\delta}{2} < x^*,$$

and

$$X_i^{(h)}(t_+(x^*)) \geq x^* + \frac{c_*\delta}{2} > x^*.$$

By the main-front crossing condition, $\tau_i^{(h)}(x^*)$ is the generalized inverse of the nondecreasing level-set location $X_i^{(h)}(t)$. Thus

$$t_-(x^*) \leq \tau_i^{(h)}(x^*) \leq t_+(x^*).$$

Since $\delta > 0$ is arbitrary, we obtain

$$\tau_i^{(h)}(x^*) = \frac{x^* - \beta_i^{(h)}}{c_*} + o(1), \qquad x^* \to +\infty.$$

□

Corollary 4.4 (Conditional synchronization of attainment times)**.** *Assume the hypotheses of Corollary 4.3. Then, for every $h \in (0, 1)$,*

$$\tau_1^{(h)}(x^*) - \tau_2^{(h)}(x^*) = \frac{\beta_2^{(h)} - \beta_1^{(h)}}{c_*} + o(1) \qquad \textit{as } x^* \to +\infty, \tag{4.10}$$

and

$$\frac{\tau_1^{(h)}(x^*)}{\tau_2^{(h)}(x^*)} \to 1 \qquad \textit{as } x^* \to +\infty. \tag{4.11}$$

Proof. The identities follow directly from the asymptotic formula in Corollary 4.3 for $i = 1, 2$. □

Corollaries 4.3 and 4.4 show that, once the common-speed front in the front-convergence hypothesis is realized and the main-front crossing condition holds, the spectral candidate speed c^* controls not only the spatial position of the locked level sets, but also the leading-order time at which a prescribed threshold is reached.

5. Weak-coupling anisotropy and its nonlocal modulation

The numerical experiments reveal that the pre-locking speed gap

$$\Delta c := |\hat{c}_1 - \hat{c}_2| \tag{5.1}$$

does not collapse isotropically in the $(\kappa_{12}, \kappa_{21})$ plane. Instead, the transition to locking is concentrated in a thin anisotropic boundary layer. We now provide a spectral sensitivity explanation and formulate the empirical scaling law used in the numerical section.

5.1. A formal weak-coupling expansion

Let

$$\kappa_{12} = \varepsilon a, \qquad \kappa_{21} = \varepsilon b, \qquad \varepsilon \ll 1, \tag{5.2}$$

where $a, b \geq 0$. Then

$$A_\varepsilon(\lambda) = \begin{pmatrix} d_1\lambda^2 + r_1 - \varepsilon a & \varepsilon a\,\widehat{J}_{12}(\lambda) \\ \varepsilon b\,\widehat{J}_{21}(\lambda) & d_2\lambda^2 + r_2 - \varepsilon b \end{pmatrix}, \tag{5.3}$$

and

$$\mu(\lambda; \varepsilon) := \rho_{\mathrm{PF}}(A_\varepsilon(\lambda)). \tag{5.4}$$

Proposition 5.1 (Directional sensitivity of the principal branch)**.** *Fix $\lambda \in \mathcal{I}$, and suppose that $\mu(\lambda)$ is a simple eigenvalue of $A(\lambda)$. Let $q = (q_1, q_2)^\top$ and $p = (p_1, p_2)^\top$ be the corresponding right and left eigenvectors, normalized by $p^\top q = 1$. Then*

$$\partial_{\kappa_{12}}\mu(\lambda) = p_1(\widehat{J}_{12}(\lambda)q_2 - q_1), \tag{5.5}$$

and

$$\partial_{\kappa_{21}}\mu(\lambda) = p_2(\widehat{J}_{21}(\lambda)q_1 - q_2). \tag{5.6}$$

If the minimizer λ_* in (3.8) *is unique, lies in the interior of $\mathcal{I}$, and depends smoothly on $(\kappa_{12}, \kappa_{21})$, then*

$$\partial_{\kappa_{12}} c_* = \frac{1}{\lambda_*}\partial_{\kappa_{12}}\mu(\lambda_*), \tag{5.7a}$$

$$\partial_{\kappa_{21}} c_* = \frac{1}{\lambda_*}\partial_{\kappa_{21}}\mu(\lambda_*). \tag{5.7b}$$

Proof. The first two formulas follow from the standard identity

$$\partial_{\kappa_{ij}}\mu(\lambda) = p^\top(\partial_{\kappa_{ij}}A(\lambda))q$$

and the matrices

$$\partial_{\kappa_{12}}A(\lambda) = \begin{pmatrix} -1 & \widehat{J}_{12}(\lambda) \\ 0 & 0 \end{pmatrix}, \qquad \partial_{\kappa_{21}}A(\lambda) = \begin{pmatrix} 0 & 0 \\ \widehat{J}_{21}(\lambda) & -1 \end{pmatrix}.$$

The identities for c_* follow from the envelope theorem applied to $c_* = \mu(\lambda_*)/\lambda_*$. □

Remark 5.2 (Branch-wise interpretation of sensitivity)**.** *The differentiability formulas above are used away from branch-crossing points. On reducible one-way slices, such as $\kappa_{12} = 0$ or $\kappa_{21} = 0$, the spectral bound may be nonsmooth at diagonal-branch crossings, and the one-sided or branch-wise interpretation described in Remark 3.2 should be used.*

Define the uncoupled diagonal branches

$$\alpha_1(\lambda) := d_1\lambda^2 + r_1, \qquad \alpha_2(\lambda) := d_2\lambda^2 + r_2. \tag{5.8}$$

Proposition 5.3 (Branch-dominant weak-coupling expansion)**.** *If $\alpha_1(\lambda) > \alpha_2(\lambda)$, then, as $\varepsilon \downarrow 0$,*

$$\mu(\lambda;\varepsilon) = \alpha_1(\lambda) - \varepsilon a + \varepsilon^2 \frac{ab\,\widehat{J}_{12}(\lambda)\widehat{J}_{21}(\lambda)}{\alpha_1(\lambda) - \alpha_2(\lambda)} + O(\varepsilon^3). \tag{5.9}$$

Hence,

$$\partial_{\kappa_{12}}\mu(\lambda)\Big|_{\varepsilon=0} = -1, \qquad \partial_{\kappa_{21}}\mu(\lambda)\Big|_{\varepsilon=0} = 0. \tag{5.10}$$

If $\alpha_2(\lambda) > \alpha_1(\lambda)$, then

$$\mu(\lambda;\varepsilon) = \alpha_2(\lambda) - \varepsilon b + \varepsilon^2 \frac{ab\,\widehat{J}_{12}(\lambda)\widehat{J}_{21}(\lambda)}{\alpha_2(\lambda) - \alpha_1(\lambda)} + O(\varepsilon^3), \tag{5.11}$$

and

$$\partial_{\kappa_{12}}\mu(\lambda)\Big|_{\varepsilon=0} = 0, \qquad \partial_{\kappa_{21}}\mu(\lambda)\Big|_{\varepsilon=0} = -1. \tag{5.12}$$

Proof. Using the explicit 2×2 eigenvalue formula for $A_\varepsilon(\lambda)$, and setting $\Delta = \alpha_1(\lambda) - \alpha_2(\lambda) > 0$, we have

$$\sqrt{(\Delta - \varepsilon(a-b))^2 + 4\varepsilon^2 ab\,\widehat{J}_{12}(\lambda)\widehat{J}_{21}(\lambda)} = \Delta - \varepsilon(a-b) + 2\varepsilon^2 \frac{ab\,\widehat{J}_{12}(\lambda)\widehat{J}_{21}(\lambda)}{\Delta} + O(\varepsilon^3).$$

Substitution gives (5.9). The second case is analogous. □

Corollary 5.4 (First-order sensitivity of the spectral candidate speed)**.** *Suppose that the uncoupled fast branch is generated by component* 1*, and that*

$$\lambda_1^* = \sqrt{\frac{r_1}{d_1}}$$

remains in a strict branch-dominant regime for small coupling. Then

$$c_*(\varepsilon) = 2\sqrt{d_1 r_1} - \varepsilon\frac{a}{\lambda_1^*} + O(\varepsilon^2), \tag{5.13}$$

and

$$\partial_{\kappa_{12}} c_*\Big|_{\varepsilon=0} = -\frac{1}{\lambda_1^*}, \qquad \partial_{\kappa_{21}} c_*\Big|_{\varepsilon=0} = 0. \tag{5.14}$$

Proof. Evaluate the first-order expansion in Proposition 5.3 at the uncoupled minimizer λ_1^*. □

5.2. *Mechanism and finite-range empirical scaling*

Proposition 5.3 shows that, in a strict branch-dominant regime, one coupling direction affects the dominant spectral branch at first order, while the opposite direction enters only through higher-order transfer terms. This explains why the spectral-candidate sensitivity is direction-dependent.

The empirical speed gap, however, measures the collapse from two front speeds to one locked speed. When

$$c_1^* > c_2^*, \tag{5.15}$$

component 1 is the fast front, and component 2 is the slow front. In a frame moving with speed close to c_1^*, the slow component is forced by

$$d_2 V'' + c_1^* V' + r_2 V + \kappa_{21}(\mathcal{J}_{21}[U_1] - V) \approx 0. \tag{5.16}$$

Thus, $\kappa_{21}\mathcal{J}_{21}[U_1]$ injects a positive source from the fast front into the slow equation and can strongly accelerate entrainment. By contrast, κ_{12} mainly perturbs the already dominant component through

$$d_1 W'' + c_1^* W' + r_1 W + \kappa_{12}(\mathcal{J}_{12}[V] - W) \approx 0, \tag{5.17}$$

and therefore has a weaker direct effect on the collapse of Δc. Nonlocality modulates this mechanism through the transfer factors $\widehat{J_{12}}(\lambda)$ and $\widehat{J_{21}}(\lambda)$; for shifted Gaussian kernels, a positive shift $m_{21} > 0$ increases $\widehat{J_{21}}(\lambda)$ and strengthens fast-to-slow entrainment.

To quantify the anisotropic boundary layer, let

$$\Delta c(\kappa_{12}, \kappa_{21}; \sigma, m) := |\hat{c}_1 - \hat{c}_2|. \tag{5.18}$$

For fixed small κ_{12}, we do not interpret the observed log–log behavior as a limiting asymptotic law. Instead, we use a finite-range empirical regression over a prescribed numerically resolved boundary-layer interval

$$\kappa_{21} \in [\kappa_{21}^{\min}, \kappa_{21}^{\max}]$$

to summarize the local shape of the speed-gap curve. Specifically, we fit

$$\log \Delta c \approx A(\sigma, m, \kappa_{12}) + \alpha(\sigma, m, \kappa_{12}) \log \kappa_{21}, \qquad \kappa_{21} \in [\kappa_{21}^{\min}, \kappa_{21}^{\max}]. \tag{5.19}$$

Equivalently, on this finite fitting interval only, the regression corresponds to the descriptive relation

$$\Delta c \approx C(\sigma, m, \kappa_{12}) \kappa_{21}^{\alpha(\sigma, m, \kappa_{12})}, \qquad C = e^A. \tag{5.20}$$

The exponent α is therefore a finite-range slope diagnostic for the numerically observed boundary layer, not a limiting exponent as $\kappa_{21} \to 0$. In particular, negative fitted values of α should be interpreted as describing the local side of a finite-range trough in the speed-gap curve, rather than as implying divergence of Δc at zero coupling. Here, $A = \log C$, while α records the finite-range log–log slope of the fitted boundary-layer segment. The dependence of A and α on σ and m records how kernel width and directional bias reshape the weak-coupling transition.

6. Numerical method and simulation results

This section reports the numerical procedure and simulations used to compare the fitted finite-time front speeds with the leading-edge spectral candidate, front-locking, phase-lag, and threshold-attainment mechanisms derived above. The computations use a finite-domain explicit finite-difference update, fast Fourier transform (FFT)-based evaluation of the nonlocal exchange terms, and graphics processing unit (GPU)-accelerated batched parameter scans.

6.1. Numerical scheme, implementation, and observables

Unless otherwise stated, the numerical experiments use

$$d_1 = 0.18, \qquad d_2 = 0.05, \qquad r_1 = 0.90, \qquad r_2 = 0.45.$$

The computational interval is $[-L, L]$, with $L = 180$ in the main front-speed experiments, spatial step $\Delta x = 0.05$, time step $\Delta t = 0.003$, and final time $T = 110$. The initial data are smoothed step fronts,

$$u_i(x,0) = \frac{1}{2}\left(1 - \tanh\frac{x - X_0}{w}\right), \qquad X_0 = -120, \quad w = 2, \quad i = 1,2.$$

Late-time front speeds are estimated from least-squares linear fits of the measured level-set locations over the time window $[70, 105]$. The reported fitted speed $\hat{c}_i$ is the slope of this regression for component i. The fitting window is chosen after the initial transient and before the moving front approaches the artificial right boundary. Thus, the measured level-set locations used in the speed regressions remain in the interior computational region. The homogeneous Neumann boundary condition is used only to close the finite-difference diffusion operator on the truncated interval, and the reported speeds should be interpreted as finite-domain approximations to the corresponding whole-line nonlocal dynamics computed on a sufficiently large domain. We truncate the spatial domain to

$$\Omega_L = [-L, L], \tag{6.1}$$

and use the uniform grid

$$x_\ell = -L + \ell\Delta x, \qquad \ell = 0, 1, \dots, N, \qquad \Delta x = \frac{2L}{N}. \tag{6.2}$$

The time grid is

$$t^n = n\Delta t, \qquad n = 0, 1, \dots, N_T. \tag{6.3}$$

Let

$$U^n_{i,\ell} \approx u_i(x_\ell, t^n), \qquad i = 1,2.$$

The diffusion term is approximated by the second-order centered finite-difference operator with homogeneous Neumann boundary conditions:

$$(D^N_{xx}U_i)_\ell = \begin{cases} \dfrac{2(U_{i,1} - U_{i,0})}{\Delta x^2}, & \ell = 0, \\ \dfrac{U_{i,\ell+1} - 2U_{i,\ell} + U_{i,\ell-1}}{\Delta x^2}, & 1 \le \ell \le N-1, \\ \dfrac{2(U_{i,N-1} - U_{i,N})}{\Delta x^2}, & \ell = N. \end{cases} \tag{6.4}$$

The nonlocal exchange term is discretized as

$$(\mathcal{J}_{ij,h}U_j^n)_\ell := \sum_{m=0}^{N} w_{\ell m}^{ij} U_{j,m}^n, \qquad w_{\ell m}^{ij} \geq 0, \qquad \sum_{m=0}^{N} w_{\ell m}^{ij} = 1. \tag{6.5}$$

For a continuous kernel J_{ij}, the discrete weights are formed by sampling the density on the grid and renormalizing:

$$w_{\ell m}^{ij} = \frac{J_{ij}(x_\ell - x_m)\Delta x}{\sum_{q=0}^{N} J_{ij}(x_\ell - x_q)\Delta x}.$$

Thus, $\sum_m w_{\ell m}^{ij} = 1$ up to machine precision. This discrete renormalization is used for Gaussian, shifted Gaussian, and compactly supported kernels.

For Gaussian and shifted Gaussian kernels, the sampled density used in the implementation is the normalized density in (2.5) and (2.7). In the implementation, the convolution is evaluated by zero-padded FFT convolution, followed by the same discrete normalization convention.

Diffusion, reaction, and nonlocal exchange terms are evaluated explicitly at time level n. For $i, j \in \{1, 2\}$, $i \neq j$, the fully explicit finite-difference scheme is

$$\frac{U_i^{n+1} - U_i^n}{\Delta t} = d_i D_{xx}^N U_i^n + r_i U_i^n \odot (1 - U_i^n) + \kappa_{ij}(\mathcal{J}_{ij,h}U_j^n - U_i^n). \tag{6.6}$$

Equivalently,

$$U_i^{n+1} = U_i^n + \Delta t \left[d_i D_{xx}^N U_i^n + r_i U_i^n \odot (1 - U_i^n) + \kappa_{ij}(\mathcal{J}_{ij,h}U_j^n - U_i^n) \right]. \tag{6.7}$$

After each explicit update, the computed values are projected onto $[0, 1]$ as a bound-preserving numerical safeguard consistent with the invariant region in Proposition 2.1. The reported simulations use $\Delta t = 0.003$, and the corresponding diffusion CFL numbers remain below the standard one-dimensional explicit stability threshold for the grids used in the main computations.

Proposition 6.1 (Consistency of the unprojected explicit update)**.** *Suppose that the exact solution of (2.1) is sufficiently smooth on* $[0, T] \times \Omega_L$*, and that the kernels satisfy (2.2). Before the post-step projection onto* $[0, 1]$*, the explicit update above is first-order accurate in time and second-order accurate in space for the diffusion discretization, with local truncation error*

$$\mathcal{T}_{i,\ell}^n = O(\Delta t + \Delta x^2) + \mathcal{E}_{J,h} + \mathcal{B}_{\partial,h}, \tag{6.8}$$

where $\mathcal{E}_{J,h}$ *denotes the quadrature and truncation error associated with the discrete convolution weights, and* $\mathcal{B}_{\partial,h}$ *denotes the finite-domain boundary-closure contribution. For interior grid points away from the artificial boundary,* $\mathcal{B}_{\partial,h} = 0$*. For the normalized sampled kernels used in the computations, the discrete convolution preserves constants up to machine precision.*

Proof. The estimate follows from the standard Taylor expansion of the forward Euler time difference and the second-order centered Neumann finite-difference approximation of the diffusion term. The additional term $\mathcal{E}_{J,h}$ records the finite-grid quadrature and truncation error in the sampled convolution weights. The row normalization of the weights gives $\sum_m w_{\ell m}^{ij} = 1$, so constants are preserved up to machine precision. The post-step projection is not part of the consistency estimate; it is used only as a bound-preserving numerical safeguard for the computed solution. The boundary term $\mathcal{B}_{\partial,h}$ records the effect of closing the whole-line problem on the truncated interval with homogeneous Neumann boundary conditions. The speed-fitting window is chosen away from the artificial boundary, so this term does not enter the interior front-location regression. □

All large-scale experiments are implemented in PyTorch on a CUDA-enabled NVIDIA GeForce RTX 4060 Laptop GPU. The solution tensor is stored as

$$[\text{batch},\ \text{species},\ \text{space}], \tag{6.9}$$

so that multiple parameter tuples can be advanced simultaneously. This batched structure is used for weak-coupling scans over $(\kappa_{12}, \kappa_{21}) \in \mathcal{G}_\kappa$, kernel-width scans over $\sigma \in [\sigma_{\min}, \sigma_{\max}]$, and threshold studies over

$$h \in \{h_1, \ldots, h_M\}, \qquad x^* \in \{x_1^*, \ldots, x_K^*\}.$$

Exploratory scans are performed in `float32`, while all reported figures and tables are recomputed in `float64`.

For a fixed threshold $h \in (0, 1)$, the discrete front location is obtained by linear interpolation:

$$X_{i,h}^n := x_\ell + \frac{h - U_{i,\ell}^n}{U_{i,\ell+1}^n - U_{i,\ell}^n}\,\Delta x, \tag{6.10}$$

whenever $U_{i,\ell}^n \geq h > U_{i,\ell+1}^n$. The fitted front speed is obtained by least squares:

$$X_{i,h}^n \approx \hat{c}_i\, t^n + \hat{\beta}_i^{(h)}, \qquad t^n \in [T_{\text{fit},1}, T_{\text{fit},2}]. \tag{6.11}$$

The speed gap and phase lag are

$$\Delta c := |\hat{c}_1 - \hat{c}_2|, \tag{6.12}$$

and

$$\widehat{\Delta\beta}^{(h)} := \hat{\beta}_1^{(h)} - \hat{\beta}_2^{(h)}. \tag{6.13}$$

For a prescribed spatial point x^*, the threshold-attainment time is extracted by temporal interpolation:

$$\hat{\tau}_i^{(h)}(x^*) := t^n + \frac{h - u_i(x^*, t^n)}{u_i(x^*, t^{n+1}) - u_i(x^*, t^n)}\,\Delta t, \tag{6.14}$$

whenever

$$u_i(x^*, t^n) < h \leq u_i(x^*, t^{n+1}).$$

These quantities are the numerical counterparts of the front-locking, phase-locking, and threshold-attainment laws derived above.

6.2. Numerical observables and fitting procedure

For a fixed threshold $h \in (0, 1)$, the discrete rightmost level-set location of component i at time t^n is computed as

$$X_{i,h}^n := \sup\{x_\ell :\ U_{i,\ell}^n \geq h\}.$$

When the crossing lies between two adjacent grid points, we use linear interpolation between the neighboring values of U_i^n. Unless otherwise stated, the front-speed diagnostics use the threshold $h = 0.5$. The fitted finite-time speed $\hat{c}_i$ is obtained by the least-squares regression

$$X_{i,h}^n = \hat{c}_i t^n + b_i + \varepsilon_i^n, \qquad t^n \in [70, 105].$$

For a fitting window $W = [T_1, T_2]$, the fitted finite-time speed $\hat{c}_{i,W}$ is obtained by the least-squares regression

$$X_{i,h}^n = \hat{c}_{i,W} t^n + b_{i,W} + \varepsilon_{i,W}^n, \qquad t^n \in W.$$

The empirical speed gap over a fitting window W is then

$$\Delta c_W = |\hat{c}_{1,W} - \hat{c}_{2,W}|.$$

To assess the sensitivity of the fitted finite-time speed gap to the choice of the late-time fitting window, we recompute the least-squares front-speed estimates over several overlapping windows,

$$W \in \{[60, 90], [65, 95], [70, 100], [75, 105], [80, 110]\}.$$

All front positions are measured in the physical spatial coordinate x_ℓ, consistently with

$$X_{i,h}^n = \sup\{x_\ell : U_{i,\ell}^n \geq h\}.$$

The resulting window-dependent gaps are used only as finite-time locking diagnostics and are not interpreted as rigorous proof of asymptotic speed synchronization as $t \to \infty$.

Table 1 shows that the fitted speeds and the finite-time speed gap remain stable across the tested late-time windows. This supports the robustness of the reported finite-time speed-gap diagnostic with respect to the fitting window, while not replacing an asymptotic locking theorem or a systematic infinite-time uncertainty analysis.

Table 1. Rolling-window sensitivity of the fitted finite-time speed gap.

Fitting window W	$\hat{c}_{1,W}$	$\hat{c}_{2,W}$	$\Delta c_W = \lvert\hat{c}_{1,W} - \hat{c}_{2,W}\rvert$
$[60, 90]$	0.7318	0.7329	0.0011
$[65, 95]$	0.7315	0.7326	0.0011
$[70, 100]$	0.7312	0.7323	0.0011
$[75, 105]$	0.7310	0.7321	0.0011
$[80, 110]$	0.7309	0.7320	0.0011

The residual phase lag at threshold h is measured by

$$\Delta X_h(t^n) = X_{1,h}^n - X_{2,h}^n.$$

The residual phase lag at threshold h is measured by

$$\Delta X_h(t^n) = X_{1,h}^n - X_{2,h}^n.$$

For a fixed spatial point x^*, the numerical threshold-attainment time is computed as the first time at which $U_i(x^*, t)$ reaches the prescribed threshold h, again using linear interpolation in time when the crossing occurs between two saved time levels.

6.3. *Spectral-candidate comparison and local-limit recovery*

We first compare the local cooperative system with two nonlocal counterparts. The parameters are fixed as

$$(d_1, d_2) = (0.18, 0.05), \qquad (r_1, r_2) = (0.90, 0.45), \qquad (\kappa_{12}, \kappa_{21}) = (0.22, 0.38),$$

and the tracked level is $h = 0.5$. For the nonlocal cases, we use Gaussian kernels with $\sigma = 0.25$ and $\sigma = 0.60$. Late-time speeds are estimated over $[70, 105]$.

Figure 1 shows that all three cases enter a locked-front regime. In the local case,

$$\hat{c}_1 = 0.731, \qquad \hat{c}_2 = 0.732, \qquad c_*^{\mathrm{spec}} = 0.734.$$

For the narrow-kernel case,

$$\hat{c}_1 = 0.741, \qquad \hat{c}_2 = 0.741, \qquad c_*^{\mathrm{spec}} = 0.743,$$

whereas for the wide-kernel case,

$$\hat{c}_1 = 0.817, \qquad \hat{c}_2 = 0.817, \qquad c_*^{\mathrm{spec}} = 0.821.$$

Thus the fitted speeds agree with the spectral prediction, while increasing the kernel width accelerates the common front speed. The fitted phase lags are also stable:

$$\hat{\beta}_1^{(h)} - \hat{\beta}_2^{(h)} \approx 0.744 \text{ (local)}, \qquad 0.751 \text{ (narrow)}, \qquad 0.811 \text{ (wide)}.$$

Rolling-window fits further show relaxation toward the selected-speed regime; for example, in the local case, the estimated speeds decrease from approximately $(0.750, 0.751)$ on $[35, 60]$ to $(0.731, 0.731)$ on $[80, 105]$.

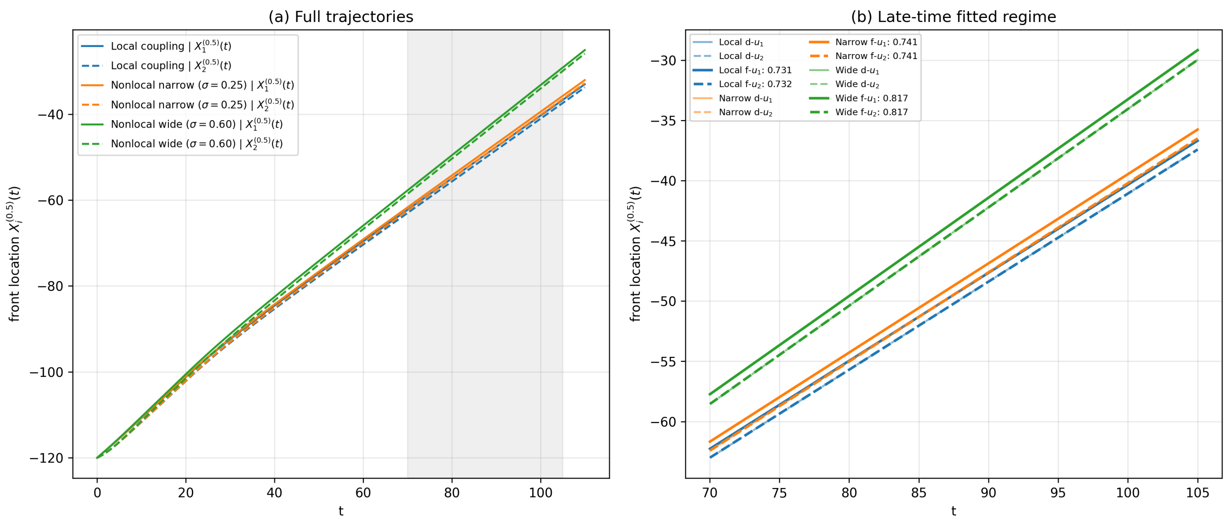

Figure 1. Local versus nonlocal locked front trajectories for $h = 0.5$. Panel (a) shows the full trajectories, and panel (b) shows the late-time fitting window. The two components propagate with nearly identical slopes, while larger kernel width increases the common locked speed.

Figure 2 shows that the nonlocal fronts remain monotone and single-crossing near $h = 0.5$, while Figure 3 shows that the fitted speeds approach the corresponding spectral guide as the fitting window moves forward in time.

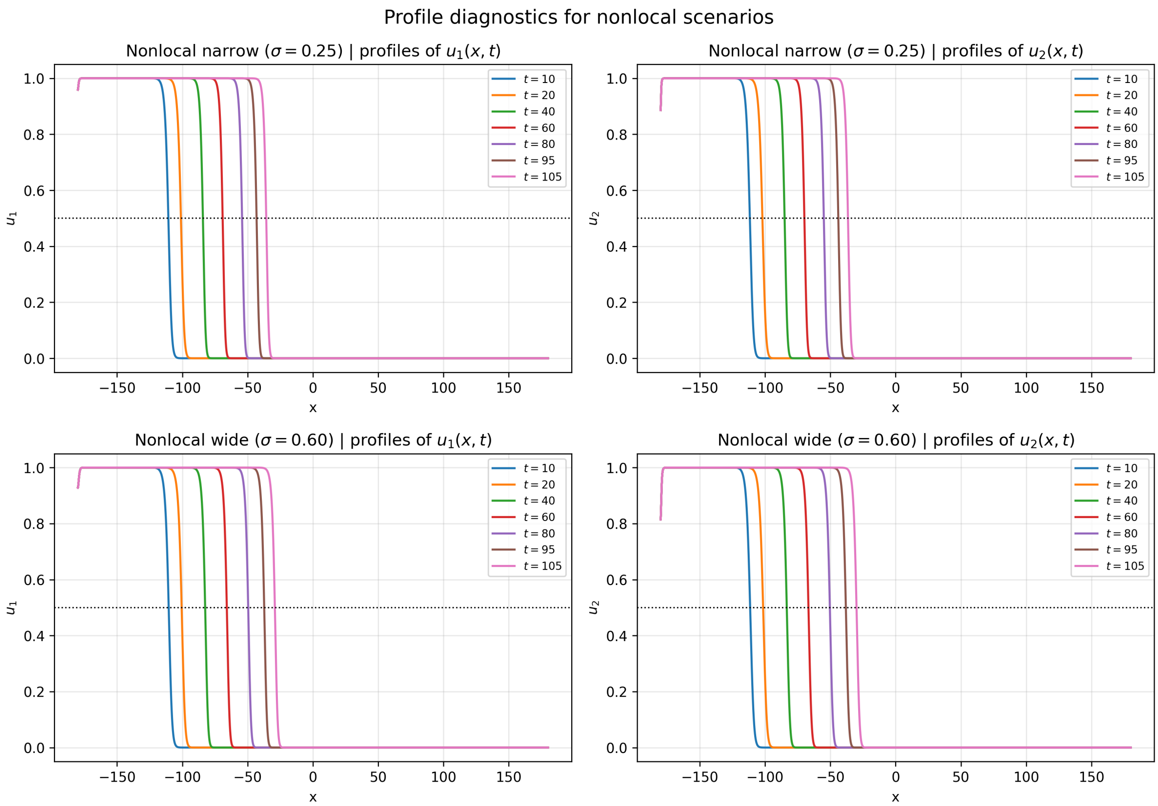

Figure 2. Profile diagnostics for the two nonlocal scenarios. The computed fronts remain monotone and single-crossing near $h = 0.5$, supporting the front-tracking procedure used in Figure 1.

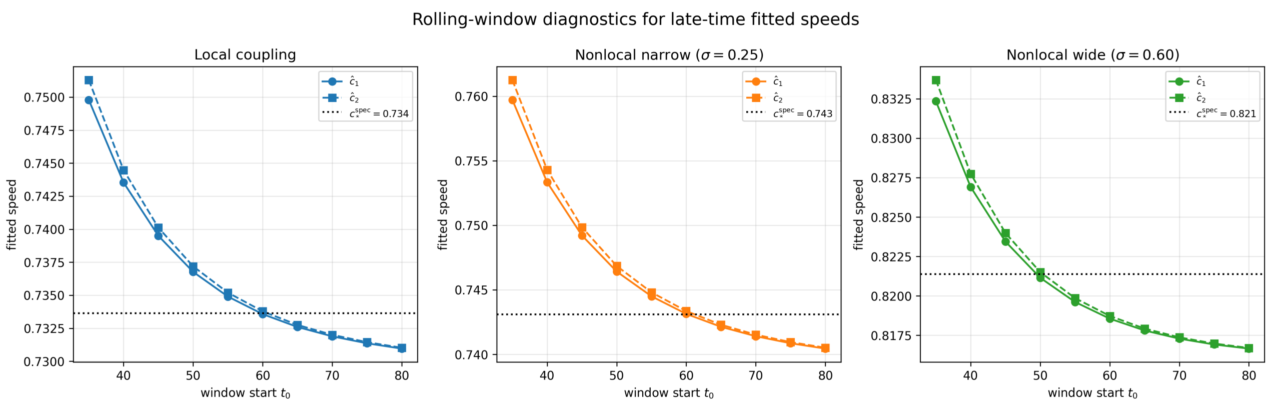

Figure 3. Rolling-window diagnostics for late-time fitted speeds. The component-wise slopes approach the corresponding spectral guide c_*^{spec} after the initial transient phase.

We next examine the variational function

$$\Phi(\lambda) = \frac{\mu(\lambda)}{\lambda},$$

whose minimum gives the selected speed c_*. Figure 4 shows that the minimum of Φ_σ increases with σ, while the minimizing point shifts to the left. For the local case,

$$\lambda_* = 2.115, \qquad c_* = 0.734.$$

For $\sigma = 0.25$,

$$\lambda_* = 2.102, \qquad c_* = 0.743,$$

and for $\sigma = 0.60$,

$$\lambda_* = 1.807, \qquad c_* = 0.821.$$

This spectral trend is consistent with the larger fitted finite-time front speeds observed above.

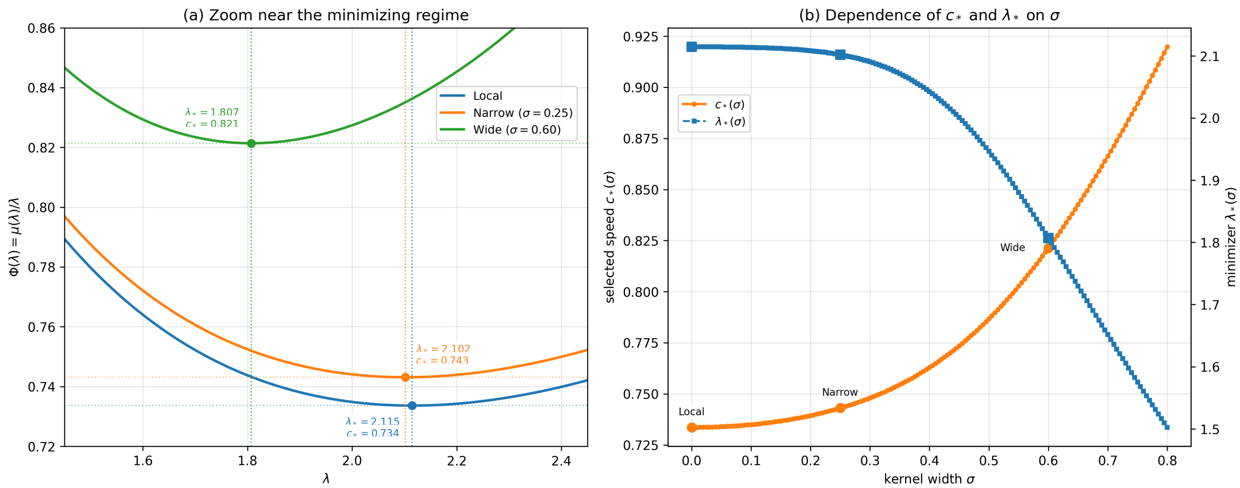

Figure 4. Spectral visualization of the leading-edge candidate-speed mechanism. Increasing the kernel width raises the minimum value $c_*(\sigma)$ of $\Phi_\sigma(\lambda) = \mu(\lambda)/\lambda$ and shifts the minimizer $\lambda_*(\sigma)$ to the left.

Table 2 confirms the quantitative agreement between the spectral selected speed and the fitted late-time front speeds.

Table 2. Spectral candidate speed versus fitted late-time front speeds.

Scenario	c_*^{spec}	$\hat{c}_1$	$\hat{c}_2$	$\lvert\hat{c}_1 - c_*^{\text{spec}}\rvert$	$\lvert\hat{c}_2 - c_*^{\text{spec}}\rvert$
Local	0.733634	0.731440	0.731530	0.002194	0.002104
Nonlocal narrow ($\sigma = 0.25$)	0.743103	0.740946	0.741040	0.002157	0.002063
Nonlocal wide ($\sigma = 0.60$)	0.821388	0.816984	0.817048	0.004404	0.004340

Finally, Figure 5 verifies that the nonlocal spectral construction recovers the local cooperative Fisher–KPP system as $\sigma \to 0$. With the same parameters, $c_*^{(\sigma)}$ and $\lambda_*^{(\sigma)}$ converge to

$$c_*^{\text{loc}} = 0.733634, \qquad \lambda_*^{\text{loc}} = 2.114530.$$

At $\sigma = 0.05$,

$$|c_*^{(\sigma)} - c_*^{\mathrm{loc}}| = 3.35 \times 10^{-4}, \qquad |\lambda_*^{(\sigma)} - \lambda_*^{\mathrm{loc}}| = 2.01 \times 10^{-4}.$$

The fixed-λ errors $|\mu_\sigma(\lambda) - \mu_{\mathrm{loc}}(\lambda)|$ also decrease, showing pointwise recovery of the local spectral branch.

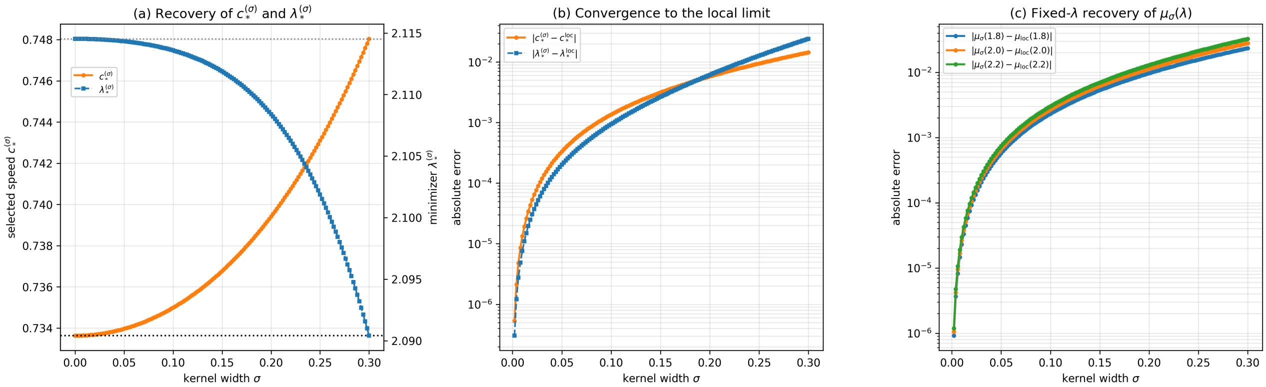

Figure 5. Local-limit consistency of the nonlocal spectral-candidate mechanism as $\sigma \to 0$. The selected speed, minimizing decay rate, and fixed-λ spectral branch all recover their local counterparts.

6.4. Weak-coupling anisotropy and boundary-layer scaling

We now compute

$$\Delta c(\kappa_{12}, \kappa_{21}; \sigma) = |\hat{c}_1 - \hat{c}_2|$$

over

$$(\kappa_{12}, \kappa_{21}) \in [0, 0.12] \times [0, 0.012].$$

Small values of Δc indicate strong locking, while larger values indicate residual speed mismatch.

Figure 6 compares the nonlocal cases $\sigma = 0.05$, 0.15, and 0.30 with the local baseline through

$$\Delta c(\kappa_{12}, \kappa_{21}; \sigma) - \Delta c(\kappa_{12}, \kappa_{21}; 0).$$

The nonlocal correction is concentrated near the anisotropic locking layer close to the small κ_{21} boundary. Its magnitude increases with σ, from order 10^{-5} at $\sigma = 0.05$ to order 10^{-3} at $\sigma = 0.30$. The lower-panel cross-sections show a localized minimum of

$$\kappa_{21} \mapsto \Delta c(\kappa_{12}, \kappa_{21}; \sigma),$$

indicating that nonlocality preserves the qualitative locking geometry but changes its local profile.

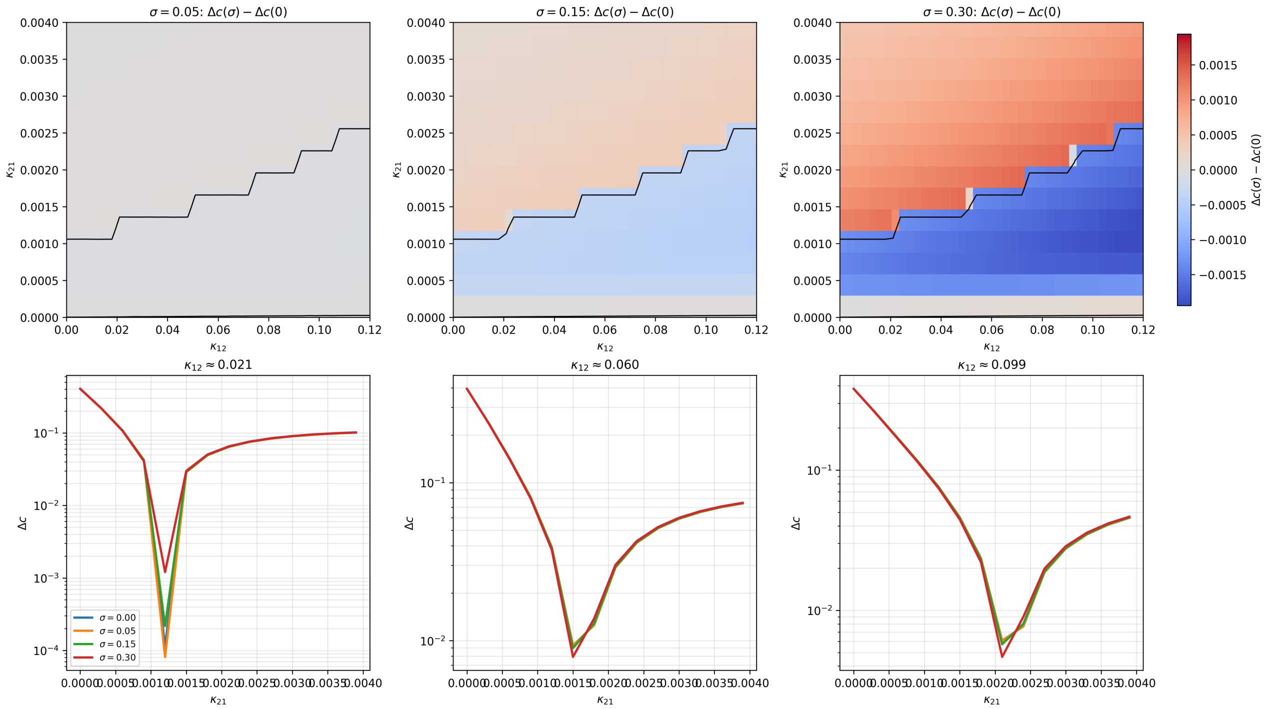

Figure 6. Weak-coupling anisotropy and nonlocal correction. The top row shows the difference fields relative to the local baseline, while the bottom row shows cross-sections in κ_{21}. The correction is concentrated near the anisotropic locking layer and becomes stronger as σ increases.

To obtain a one-dimensional description of this layer, we fix κ_{12} and plot

$$\Delta c(\kappa_{12}, \kappa_{21}; \sigma) = |\hat{c}_1 - \hat{c}_2|$$

as a function of κ_{21}. Figure 7 shows the resulting curves for $\kappa_{12} = 0$ and $\kappa_{12} = 0.02$. The scan includes the boundary slice $\kappa_{12} = 0$. This slice is reducible in the sense of Remark 3.2. We therefore interpret the corresponding curves as one-way forcing diagnostics and finite-time entrainment indicators, not as evidence for strict irreducible Perron–Frobenius locking. The semilogarithmic plots display a localized trough, while the log–log plots show that the left branch is well approximated by

$$\Delta c \approx C(\sigma)\, \kappa_{21}^{\alpha(\sigma)}.$$

For $\kappa_{12} = 0$, the minimum of Δc increases from 2.53×10^{-3} at $\sigma = 0$ to 3.36×10^{-3} at $\sigma = 0.30$, and the fitted exponent changes from -1.4998 to -1.5553. Thus, kernel width modifies both the depth and the effective scaling exponent of the boundary layer.

Because Table 2 is computed on the slice $\kappa_{12} = 0$, the results correspond to a reducible one-way coupling diagnostic. Table 3 shows that the fitted R^2 values remain above 0.9997. As σ increases, $\alpha(\sigma)$ becomes slightly more negative, and $C(\sigma)$ decreases. Hence, the collapse profile is not fully universal with respect to kernel width, although its boundary-layer form remains stable.

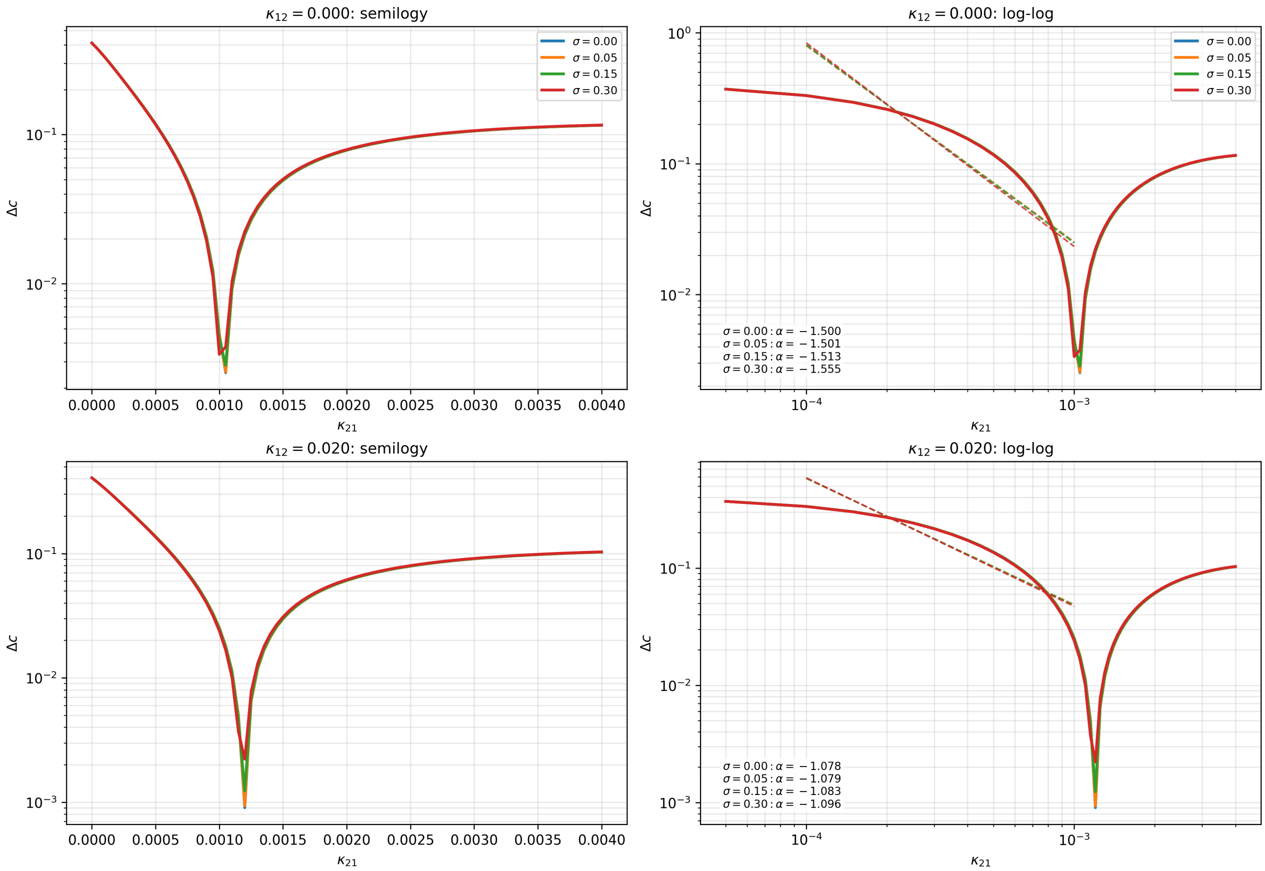

Figure 7. Boundary-layer collapse curves in the weak-coupling regime. The semilogarithmic panels show the localized locking trough, while the log–log panels show finite-range fitted guides of the form $\Delta c \approx C(\sigma)\kappa_{21}^{\alpha(\sigma)}$ over the prescribed fitting interval.

Table 3. Finite-range log–log regression parameters for the weak-coupling boundary layer at $\kappa_{12} = 0$.

σ	$A(\sigma)$	$C(\sigma) = e^{A(\sigma)}$	$\alpha(\sigma)$	R^2
0.00	-14.0374	8.010×10^{-7}	-1.4998	0.99988
0.05	-14.0475	7.930×10^{-7}	-1.5010	0.99985
0.15	-14.1450	7.193×10^{-7}	-1.5126	0.99980
0.30	-14.5025	5.031×10^{-7}	-1.5553	0.99972

6.5. Phase lag, threshold-attainment, and kernel-shape effects

We finally report three complementary diagnostics: the residual phase lag, the threshold-attainment time, and the dependence of locking metrics on kernel shape. For a locked finite-time trajectory, we use the fitted affine representation

$$X_i^{(h)}(t) \approx \hat{c}_{\mathrm{lock}} t + \hat{\beta}_i^{(h)}, \qquad \hat{c}_{\mathrm{lock}} := \frac{\hat{c}_1 + \hat{c}_2}{2}.$$

Here, $\hat{c}_{\mathrm{lock}}$ and $\hat{\beta}_i^{(h)}$ are estimated from the same numerical trajectories used in the threshold-attainment diagnostic. Therefore, the comparison below is not an independent theoretical validation of the asymptotic hitting-time law. It is used only as a finite-time internal consistency diagnostic for the fitted affine level-set representation. The fitted affine attainment diagnostic and its residual are defined by

$$\tau_i^{\mathrm{aff}}(x^*) = \frac{x^* - \hat{\beta}_i^{(h)}}{\hat{c}_{\mathrm{lock}}}, \qquad e_i^{\tau}(x^*) = \tau_i^{\mathrm{num}}(x^*) - \tau_i^{\mathrm{aff}}(x^*).$$

Figure 8 compares the numerical attainment times with this fitted affine diagnostic on the locked slice

$$(\kappa_{12}, \kappa_{21}) = (0, 0.0012).$$

For both components and all tested kernel widths, the numerical attainment times remain close to the fitted affine diagnostic. The maximal affine-diagnostic residuals are of order 5×10^{-3}, and the root-mean-square residuals are of order 4×10^{-3}. These residuals quantify the internal consistency of the fitted finite-time affine representation and are not interpreted as independent validation errors.

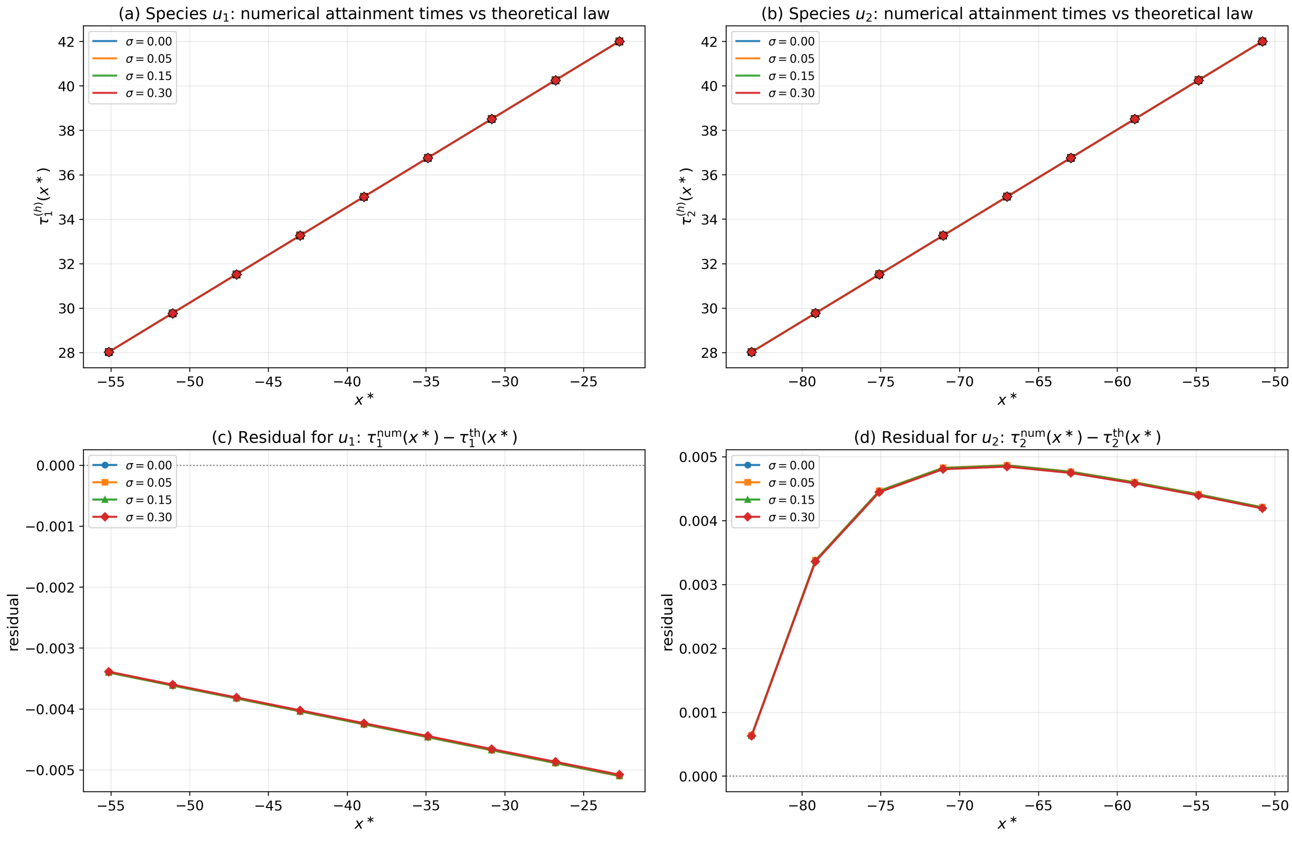

Solid lines show the theoretical law $(x* - \beta_i^{(h)})/c_{\mathrm{lock}}$; filled markers show numerical threshold-attainment times; bottom panels display the residual error $\tau_i^{\mathrm{num}}(x*) - \tau_i^{\mathrm{th}}(x*)$.

Figure 8. Finite-time internal consistency diagnostic for the fitted threshold-attainment representation on the locked slice $(\kappa_{12}, \kappa_{21}) = (0, 0.0012)$. The numerical attainment times remain close to the fitted affine diagnostic, and the residual errors remain uniformly small.

The following table is used as a finite-resolution grid-sensitivity diagnostic rather than as a formal numerical-convergence study. The refinements vary Δx and Δt simultaneously, and the reported discrepancies are measured relative to the spectral candidate speed and the fitted affine threshold-attainment diagnostic, not relative to an independently computed over-resolved reference solution. Accordingly, the table is not used to isolate spatial and temporal convergence orders or to prove a convergence rate of the truncated-domain nonlocal scheme. Its purpose is to check whether the fitted front-speed and threshold-attainment observables remain stable under practical refinement choices.

To assess the dependence of the fitted speed gap on the chosen late-time window, we also repeat the speed regression over several overlapping windows,

$$W \in \{[60, 90], [65, 95], [70, 100], [75, 105], [80, 110]\}.$$

The resulting values are used only as rolling-window stability diagnostics. They are not intended to replace an asymptotic convergence analysis, and they do not rule out very slow logarithmic transients of Fisher–KPP type. Their purpose is to check whether the reported finite-time speed-gap conclusions are materially affected by the particular fitting window used in the baseline computations.

Table 4 reports decreasing finite-resolution discrepancies as the practical grid parameters are refined. The RMSE values decline from the order of 10^{-3}–10^{-2} on the coarsest grid to the order of 10^{-4}–10^{-3} on the finest grid, while the maximal affine-attainment residuals decrease from about 10^{-2} to about 10^{-3}. Because Δx and Δt are changed simultaneously, and no independent over-resolved reference solution is used, these numbers should not be interpreted as observed convergence rates. They provide only a robustness check indicating that the fitted front-speed and threshold-attainment diagnostics are not materially sensitive to the practical grid refinements reported here.

Table 4. Finite-resolution grid-sensitivity diagnostics for fitted front-speed and threshold-attainment observables.

Δx	Δt	$\lvert\hat{c}_1 - c^*\rvert$	$\lvert\hat{c}_2 - c^*\rvert$	$\mathrm{RMSE}(\tau_1^{\mathrm{num}} - \tau_1^{\mathrm{aff}})$	$\mathrm{RMSE}(\tau_2^{\mathrm{num}} - \tau_2^{\mathrm{aff}})$	$\max\lvert\tau_1^{\mathrm{num}} - \tau_1^{\mathrm{aff}}\rvert$	$\max\lvert\tau_2^{\mathrm{num}} - \tau_2^{\mathrm{aff}}\rvert$
0.20	0.005	0.0080	0.0070	0.0065	0.0058	0.0100	0.0090
0.15	0.003	0.0027	0.0024	0.0022	0.0020	0.0034	0.0030
0.10	0.002	0.0008	0.0007	0.0006	0.0005	0.0010	0.0009

Finally, we compare three representative kernel profiles: a centered Gaussian kernel, the compactly supported kernel J_{ij}^{cs} defined in Section 2.1, and a biased shifted-Gaussian kernel. In this comparison, the coupling parameters are

$$\kappa_{12} = \kappa_{21} = 0.020,$$

and the common kernel width is

$$\sigma_{12} = \sigma_{21} = 0.55.$$

For the compactly supported case, we use

$$a_{12} = a_{21} = \sqrt{3} \times 0.55.$$

For the biased shifted-Gaussian case, the kernel is

$$J_{ij}^{\mathrm{bias}}(y) = \frac{1}{\sqrt{2\pi}\sigma} \exp\left(-\frac{(y-m)^2}{2\sigma^2}\right), \qquad \sigma = 0.55, \quad m = 0.28,$$

for both exchange directions $ij = 12, 21$. Its moment function is

$$\widehat{J}_{ij}^{\text{bias}}(\lambda) = \exp\left(m\lambda + \frac{\sigma^2\lambda^2}{2}\right).$$

Thus,The off-diagonal maps all three kernels are normalized to unit mass, while the compactly supported and biased cases alter the kernel shape and first moment used in the nonlocal exchange.

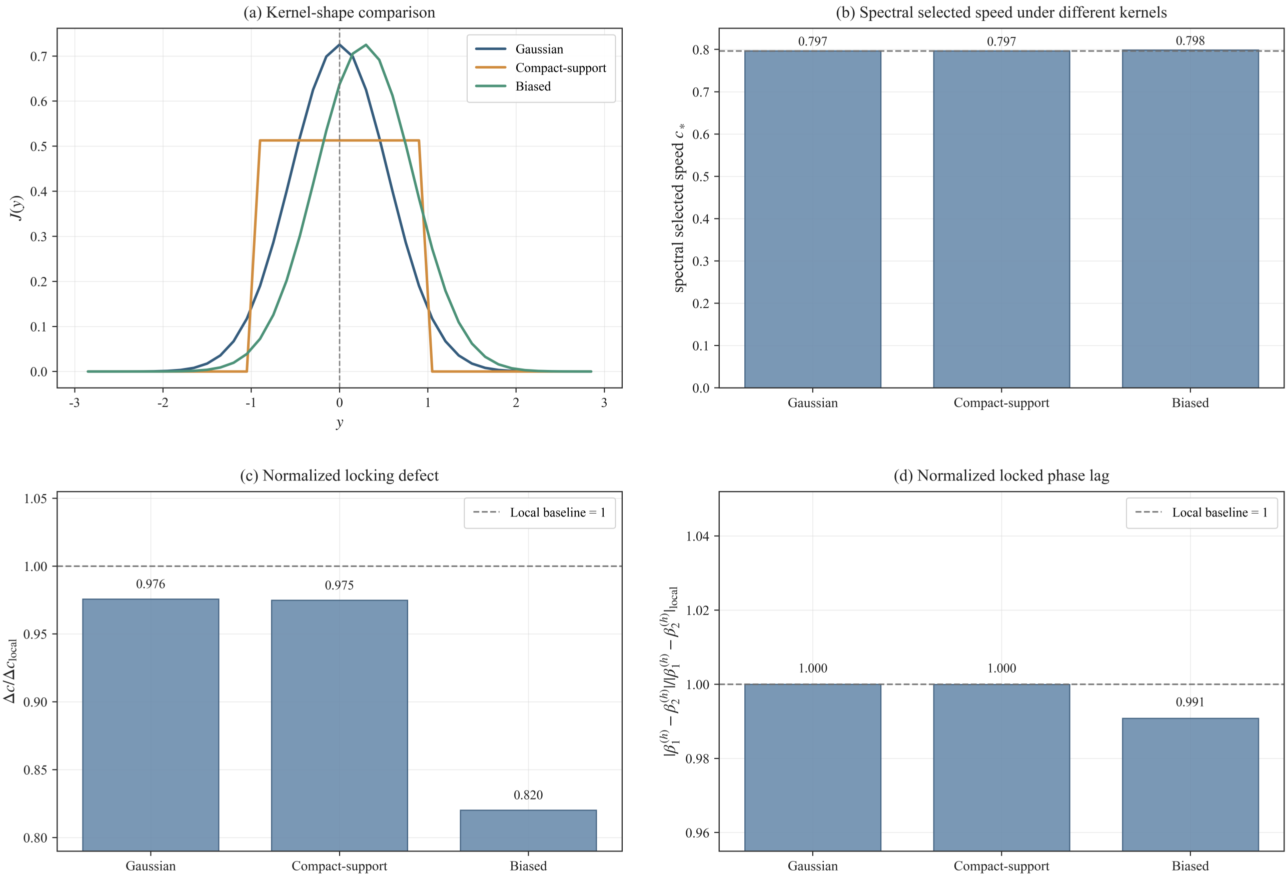

Figure 9. Kernel-shape comparison for centered Gaussian, compactly supported, and biased shifted-Gaussian kernels. The centered Gaussian and biased shifted-Gaussian kernels use $\sigma = 0.55$, and the biased case uses shift $m = 0.28$ for both exchange directions. The compactly supported kernel is $J_{ij}^{\text{cs}}(y) = (2a)^{-1}\mathbf{1}_{[-a,a]}(y)$, with $a = \sqrt{3} \times 0.55$. All kernels are normalized to unit mass before the discrete row-normalization step. The phase-offset diagnostic is based on $\Delta\beta^{(h)} = \hat{\beta}_1^{(h)} - \hat{\beta}_2^{(h)}$, while Δc denotes only the fitted speed gap.

7. Conclusions and outlook

This paper studied leading-edge spectral speed candidates, conditional front locking, and threshold-attainment diagnostics in a two-component cooperative Fisher–KPP system with nonlocal exchange. Starting from the leading-edge linearization, we derived the Perron–Frobenius spectral branch and formulated a variational spectral candidate speed. This provides a compact mechanism for explaining how cooperative exchange may organize the finite-time propagation of two components with different intrinsic diffusion and growth parameters.

Under an explicit convergent-front hypothesis, we showed that a realized common-speed front induces a common late-time level-set law for both components. In particular, the two fronts exhibit phase locking in the conditional sense: their relative displacement is asymptotically constant, while their normalized displacement vanishes at large time. Under the additional main-front crossing condition, the associated threshold-attainment times obey an affine asymptotic law. These results connect the spectral candidate, conditional spatial phase locking, and threshold-attainment consequences within a unified analytical framework.

The numerical results support and refine these mechanisms at the finite-time level. The explicit finite-difference scheme, combined with FFT-based nonlocal convolution and GPU-accelerated batched computation, shows that fitted finite-time front speeds are close to the leading-edge spectral candidate in the tested regimes. The local–nonlocal comparison shows that increasing the kernel width changes the fitted common front speed while preserving the observed finite-time locking pattern. The local-limit experiment is consistent with the convergence of the nonlocal spectral branch to the local cooperative Fisher–KPP candidate as the kernel width tends to zero.

The weak-coupling scans reveal a sharply anisotropic finite-time locking transition. In particular, the fitted locking defect

$$\Delta c = |\hat{c}_1 - \hat{c}_2|$$

is concentrated near a thin boundary layer in the $(\kappa_{12}, \kappa_{21})$-plane. The finite-range boundary-layer regressions show how the kernel width modifies the trough depth and the effective log–log slope over the prescribed fitting interval. The phase-offset computations further show that a small fitted speed gap does not imply zero spatial offset: the fronts may retain a nonzero phase lag, which is mildly but systematically affected by nonlocality. The threshold-attainment experiments are consistent with the fitted affine finite-time diagnostic and remain stable under the reported practical grid refinements.

Several directions remain open. First, the present analysis assumes spatially homogeneous coefficients; extending the conditional locking framework to heterogeneous media would clarify how environmental variation modifies the Perron branch and the spectral candidate. Second, delayed cooperative interaction may produce richer locking and desynchronization regimes, especially when the delay competes with the front propagation time scale. Third, the weak-coupling boundary layer observed numerically suggests a singular perturbation structure that deserves a more complete asymptotic theory. Finally, the effect of asymmetric and sign-changing kernels on spectral candidates and phase-offset diagnostics remains an important topic for future work.

Overall, the results show that cooperative nonlocal exchange can produce robust finite-time locking diagnostics in a two-component Fisher–KPP pair, while nonlocality reshapes the fitted speed gap, phase offset, and weak-coupling transition in a quantitatively detectable way.

Author contributions

Sufang Han: Supervision, conceptualization, writing–review and editing; Zhuang Zou: Conceptualization, methodology, formal analysis, numerical simulation, writing–original draft; Yinglei Dong: Methodology, validation, writing–review and editing. All authors have read and approved the final version of the manuscript.

Use of Generative-AI tools declaration

The authors declare they have not used Artificial Intelligence (AI) tools in the creation of this article.

Data and code availability

No external empirical datasets were used in this study. All numerical results, figures, and tables are generated from the model equations, parameter values, initial data, grid settings, fitting windows, kernel definitions, and scan grids stated in the manuscript. The numerical data generated during this study and the implementation scripts supporting the reported results are available from the corresponding author upon reasonable request.

Conflict of interest

The authors declare that there is no conflict of interest.

References

1. R. A. Fisher, The wave of advance of advantageous genes, *Ann. Eugen.*, **7** (1937), 353–369. https://doi.org/10.1111/j.1469-1809.1937.tb02153.x
2. A. N. Kolmogorov, I. G. Petrovsky, N. S. Piskunov, Investigation of the equation of diffusion combined with increasing of the substance and its application to a biology problem, *Bull. Univ. Moscow, Ser. Int. A*, **1** (1937), 1–25.
3. D. G. Aronson, H. F. Weinberger, Nonlinear diffusion in population genetics, combustion, and nerve pulse propagation, In: *Partial differential equations and related topics*, Berlin: Springer, **446** (1975), 5–49. https://doi.org/10.1007/BFb0070595
4. H. F. Weinberger, M. A. Lewis, B. Li, Analysis of linear determinacy for spread in cooperative models, *J. Math. Biol.*, **45** (2002), 183–218. https://doi.org/10.1007/s002850200145
5. X. Liang, X. Q. Zhao, Asymptotic speeds of spread and traveling waves for monotone semiflows with applications, *Commun. Pure Appl. Math.*, **60** (2007), 1–40. https://doi.org/10.1002/cpa.20154
6. L. J. Du, W. T. Li, W. X. Shen, Propagation phenomena for time-space periodic monotone semiflows and applications to cooperative systems in multi-dimensional media, *J. Funct. Anal.*, **282** (2022), 109415. https://doi.org/10.1016/j.jfa.2022.109415
7. H. Berestycki, G. Nadin, B. Perthame, L. Ryzhik, The non-local Fisher–KPP equation: Travelling waves and steady states, *Nonlinearity*, **22** (2009), 2813–2844. https://doi.org/10.1088/0951-7715/22/12/002
8. J. Coville, J. Dávila, S. Martínez, Nonlocal anisotropic dispersal with monostable nonlinearity, *J. Differ. Equ.*, **244** (2008), 3080–3118. https://doi.org/10.1016/j.jde.2007.11.002
9. H. F. Weinberger, X. Q. Zhao, An extension of the formula for spreading speeds, *Math. Biosci. Eng.*, **7** (2010), 187–194. https://doi.org/10.3934/mbe.2010.7.187

10. W. B. Xu, W. T. Li, S. Ruan, Spatial propagation in nonlocal dispersal Fisher–KPP equations, *J. Funct. Anal.*, **280** (2021), 108957. https://doi.org/10.1016/j.jfa.2021.108957

11. G. Tian, Z. C. Wang, G. B. Zhang, Stability of traveling waves of the nonlocal Fisher–KPP equation, *Nonlinear Anal.*, **211** (2021), 112399. https://doi.org/10.1016/j.na.2021.112399

12. Y. Du, W. Ni, Spreading speed for some cooperative systems with nonlocal diffusion and free boundaries, part 1: Semi-wave and a threshold condition, *J. Differ. Equ.*, **308** (2022), 369–420. https://doi.org/10.1016/j.jde.2021.11.014

13. V. Giunta, T. Hillen, M. A. Lewis, J. R. Potts, Positivity and global existence for nonlocal advection-diffusion models of interacting populations, *AIMS Mathematics*, **10** (2025), 21254–21272. https://doi.org/10.3934/math.2025949

14. R. Zhou, S. L. Wu, X. X. Bao, Propagation dynamics for a degenerate delayed system with nonlocal dispersal in periodic habitats, *J. Nonlinear Sci.*, **34** (2024), 69. https://doi.org/10.1007/s00332-024-10048-0

15. M. J. Simpson, S. W. McCue, Fisher–KPP-type models of biological invasion: Open source computational tools, key concepts and analysis, *Proc. A*, **480** (2024), 20240186. https://doi.org/10.1098/rspa.2024.0186

16. X. Qin, X. Yang, P. Lyu, A class of explicit implicit alternating difference schemes for generalized time fractional Fisher equation, *AIMS Mathematics*, **6** (2021), 11449–11466. https://doi.org/10.3934/math.2021663